Numerical Investigation of the Unsteady Turbulent Wake Regimes of a Notchback Ahmed Body

Joseph Kwabena Kodie-Ampaw

A Thesis

in

The Department

of

Mechanical Industrial and Aerospace Engineering

Presented in Partial Fulfillment of the Requirements

for the Degree of

Master of Applied Science (Mechanical Engineering) at

Concordia University

Montreal, Quebec, Canada

August 2025

©Joseph Kwabena Kodie-Ampaw, 2025

Concordia University

School of Graduate Studies

	This	is	to	certify	that	the	thesis	pre	pared
--	------	----	----	---------	------	-----	--------	-----	-------

By:	Joseph Kwabena Kodie-Am	paw				
Entitled:	Numerical Investigation of the Unsteady Turbulent Wake Regimes of a Notchback Ahmed Body					
and submitted	in partial fulfillment of the re	equirements for the degree of				
	Master of Applied Sci	ience (Mechanical Engineering)				
complies with originality and	_	rsity and meets the accepted standards with respect				
Signed by the	final Examining Committee:					
		Chair				
	Dr. Jerin John					
		Examiner				
	Dr. Jerin John					
		Examiner				
	Dr. Brian Vermeire					
		Supervisor				
	Dr. Ebenezer Ekow E	Essel				
Approved by						
	Muthukumaran Pack	Muthukumaran Packirisamy, Chair				
	Department of Mech	anical, Industrial and Aerospace Engineering				
	2025					
	Moura	ad Debbabi, Dean				
	Gina G	Cody School of Engineering and Computer Science				

to

Abstract

Numerical Investigation of the Unsteady Turbulent Wake Regimes of a Notchback Ahmed Body

Joseph Kwabena Kodie-Ampaw

This study investigates the influence of Reynolds number on the unsteady turbulent wake regimes of a notchback Ahmed body with an effective backlight angle of 17.8°. Three-dimensional improved delayed detached eddy simulations (IDDES) were conducted at two Reynolds numbers, $Re_h = 1 \times 10^4$ (denoted as Re1E4) and $Re_h = 5 \times 10^4$ (Re5E4), representing symmetric and fully asymmetric flow regimes, respectively. Detailed aspects of the wake dynamics, including the mean flow, Reynolds stresses, large-scale anisotropy, global instabilities, and the pumping motion (i.e., quasi-periodic expansion and contraction) of reverse flow regions, are used to characterize the effects of Reynolds number. The results showed that, unlike Re1E4, the wake of Re5E4 is associated with asymmetric reattachment on the deck and a directional bias of the vortical structures towards one side of the body. This asymmetry significantly enhances turbulence anisotropy and causes a spanwise imbalance in turbulence production in Re5E4 compared to Re1E4. The pumping motion of the reverse flow regions was found to be synchronized between the bubbles over the slant and behind the back for Re1E4, but out of phase for Re5E4. Additionally, for Re5E4, frequent contractions on one side of the body were accompanied by expansions on the opposite side, a behavior not prevalent in Re1E4.

Acknowledgments

I sincerely thank my supervisor, Dr. Ebenezer Ekow Essel, for his invaluable guidance, support, and mentorship throughout this research journey at the Concordia Turbulence Research Laboratory (CTRL). His dedication and insights have been instrumental to both this work and my growth as a researcher.

I am also grateful to Dr. Jerin John and Dr. Brian Vermeire for serving on my thesis committee and for their thoughtful feedback.

Special thanks to my lab mates Newton, Kofi, Akili, and Ashim for their support and collaboration. I also deeply appreciate my parents and brothers, and my friends Quayson-Sackey, Paapa, and Bright, for their constant encouragement.

This thesis would not have been possible without the support and inspiration of everyone mentioned above.

Contents

Abstract	iii
Acknowledgments	iv
List of figures	vii
List of tables	ix
List of acronyms	X
Nomenclature	xi
Chapter 1	1
Introduction	1
1.2 Motivation	1
1.2 Literature review	3
1.2.1 Salient Flow Features of The Ahmed Body Wake	3
1.2.2 Geometric and Flow Parameters Influencing the Wake Dynamics	4
1.2.3 Notchback Ahmed body	7
1.3 Objective	9
1.4 Organisation	10
Chapter 2	11
Methodology	11
2.1 Governing equations	11
2.1.1 Conservation of mass	11
2.1.2 Conservation of momentum	12
2.2 Turbulence modelling	13
2.2.1 Introduction	13
2.2.2 Reynolds Averaged Navier-Stokes equations	14
2.2.2.1 Standard Spalart Allmaras (SSA) model	15
2.2.3 Scale-Resolving Simulations	16
2.2.3.1 Large Eddy Simulations (LES)	16
2.2.3.2 Detached Eddy Simulations (DES)	18
2.2.3.2.1 Improved Delayed Detached Eddy Simulations (IDDES)	19
Chanter 3	22

3.1 Introduction	22
3.2 Numerical Setup	26
3.2.1 Governing equation of the turbulence model	26
3.2.2 Computational domain, boundary conditions and test conditions	28
3.3 Results and discussion	32
3.3.1 Mean flow characteristics	32
3.3.2 Turbulence statistics	39
3.3.3 Instantaneous vortical structures and global dynamics	49
Chapter 4	60
Conclusion	60
4.1 Summary	60
4.2 Recommended future work	62
References	63

List of figures

Figure 1.1 Representation of (a) flow around a ground vehicle (b) hatchback, (c) square-back	
and (d) notchback Ahmed body with the nomenclature	
et al., 1984) by Choi et al. (2014).	
Figure 3.1: Schematic drawing of the notchback Ahmed body with the nomenclature used in present study.	
Figure 3.2: The computational domain and boundary conditions: (a) Side view of the mesh is symmetry plane $(z/h = 0)$, (b) top view of the mesh, (b) surface mesh on the rear of the Ahmed body with dots representing pressure coefficient monitoring points and two-dimensional planes used for investigations.	in the end d (d)
Figure 3.3: Profiles of mean streamwise velocity extracted in the spanwise plane at $y/h = 0.343$ and streamwise locations from $le1$ (0.03 h away from the vertical bawith an interval of 0.1 h up to $le9$. The present results for Re5E4 are compared with LES and IDDES profiles of He et al (2021), where – M and – C represent medium at coarse meshes, respective used in the previous study	the nd
Figure 3.4: Contours of normalized streamwise mean velocity, $U/U \infty$ in the symmetry plan $(z/h = 0)$ and offset planes $(z/h = \pm 0.417)$, superimposed with mean streamlines (a-c) Re1E4 and (d-f) Re5E4. The green line represents the isopleth of $U/U \infty = 0$ which bounds the reverse flow region $(U/U \infty < 0)$. The plus (+) sign shows the loc the maximum backflow velocity and the green dot (•) represents the saddle point	for eus of
Figure 3.5: Contours of normalized wall normal mean velocity $V/U\infty$, superimposed with n streamlines. The green line represents the isopleth of $U/U\infty = 0$ which bounds the reverse flow region $(U/U\infty < 0)$ and the green dot (\bullet) represents the saddle point	;
Figure 3.6: Contours of normalized spanwise mean velocity $W/U \infty$ in the horizontal planes b) at $y/h = 0.844$ and (c, d) $y/h = 0.343$ for Re1E4 and Re5E4	
Figure 3.7: Contours of the mean pressure coefficient in the cross planes at (a, b)	
$x/h = -0.717$, (c, d) $x/h = -0.234$ and (e, f) $x/h = 0.3$ for Re1E4 and Re5E4 Figure 3.8: Three-dimensional mean flow topology in the near wake of (a) Re1E4 case, and Re5E4 case, visualized using the iso-surfaces of the mean Q -criterion ($Q(h/U \infty)$) 2 3.7) and reverse flow volume ($U/U \infty = 0$, i.e., green region)	(b) =
Figure 3.9: Contours of (a) streamwise Reynolds normal stress, $u'u'$, (b) wall normal Reynon normal stress $v'v'$ and (c) spanwise Reynolds normal stress $w'w'$ in the vertical plane Re1E4 and Re5E4	es for 41
Figure 3.10: Contours of normalized Reynolds shear stress, $u'v'$ for Re1E4 and Re5E4 in t vertical planes $z/h = 0$ and $z/h = \pm 0.417$	
Figure 3.11: Contours of turbulence anisotropy, (a) $b11$, (b) $b22$ and (c) $b33$ in the vertical planes $z/h = 0$ and $z/h = \pm 0.417$ for Re1E4 and Re5E4	
Figure 3.12: Contours of normalized production of turbulence kinetic energy (Pk) in the ver planes, $z/h = 0$ and $z/h = \pm 0.417$ for Re1E4 and Re5E4	rtical
<u>.</u> , , , , , , , , , , , , , , , , , , ,	

Figure 3.13: Contours of normalized Reynolds normal stress production: (a) streamwise
production Puu, (b) wall normal production Pvv and (c) spanwise production Pww 48
Figure 3.14: Contours of Reynolds stresses (a) $u'u'$, (b) $v'v'$, (c) $w'w'$ and (d) $u'w'$ in the
spanwise planes at $y/h = 0.844$ and $y/h = 0.343$ for Re1E4 and Re5E4
Figure 3.15: Instantaneous vortical structures visualized at the normalized Q-criterion value
$Q(h/U\infty)$ 2 = 80 for Re1E4 and Re5E4 cases colored by the normalized instantaneous
spanwise velocity (w)
Figure 3.16: Temporal history ($tU \infty / h$) and probability density function (PDF) of the spanwise
gradient of pressure coefficient, $\Delta Cp/(\Delta z/h)$, on the slant, deck and back for (a) Re1E4,
(b) Re5E4, (c) drag coefficient, (d) lift coefficient and (e) drift coefficient for Re1E4 and
Re5E4
Figure 3.17: Contours of normalized instantaneous streamwise velocity $u/U \infty$ in the vertical
planes $z/h = 0$ and $z/h = \pm 0.417$ for Re1E4 and Re5E4, representing a
characteristic instantaneous flow field. Blue regions indicate reverse flow areas
$(U/U \propto < 0)$ on the slant and at the back of the Ahmed body
Figure 3.18: Contours of normalized instantaneous streamwise velocity $u/U \infty$ in the spanwise
planes at (a, b) $y/h = 0.844$ and (c, b) $y/h = 0.343$ representing a characteristic
instantaneous flow field for Re1E4 and Re5E4. The blue regions indicate reverse flow
areas $(U/U \infty < 0)$ on the slant and at the back of the Ahmed body
Figure 3.19: Time history and the probability density function (PDF) of the reverse flow area
fluctuations (A') on the (a-c) slant and (d-f) back in the vertical planes $z = 0$ and $z/h =$
± 0.417 for Re1E4 and Re5E4. The parameters Sk and K represent the skewness and
kurtosis of A', respectively
Figure 3.20: Time history and the probability density function (PDF) of the reverse flow area
fluctuations on the (a) slant mid-height $(y/h = 0.844)$ and (b) back mid-height $(y/h = 0.844)$
0.343) spanwise planes for Re1E4 and Re5E4. The parameters Sk and K represent the
skewness and kurtosis of A' , respectively
Figure 3.21: Joint probability density function (JPDF) of the fluctuations of reverse flow area on
the slant and behind the back in the vertical planes $z=0$ and $z/h=\pm0.417$ for (a)
Re1E4 and (b) Re5E4

List of tables

Table 3.1	Summary of grid properties for mesh sensitivity test of the Re5E4 simulation	30
Table 3.2	Summary of the mean reverse flow parameters for Re1E4 and Re5E4.	34

List of acronyms

2D - 2CTwo-Dimensional – Two Velocity Components

2D - 3CTwo-Dimensional – Three Velocity Components

BR Blockage ratio

CFD Computational Fluid Dynamics

DDES Delayed Detached Eddy Simulations

DES Detached Eddy Simulations

Direct Numerical Simulations DNS

GHG Greenhouse Gas

IDDES Improved Delayed Detached Eddy Simulations

LRR-IP Launder, Reece and Rodi – Isotropization of Production

PDF **Probability Density Function**

RANS Reynolds Averaged Navier-Stokes RSB

Reflectional Symmetry Breaking

SSA Standard Spalart Allmaras

SUVs Sport Utility Vehicles

TR-PIV Time-resolved Particle Image Velocimetry

URANS Unsteady Reynolds Averaged Navier-Stokes

Nomenclature

Α Mean reverse flow area A' > 0Expansion of the reverse flow region relative to A A' < 0Contraction of the reverse flow region relative to A Mean reverse flow area over the slant A_r Mean reverse flow area behind the back A_R Instantaneous reverse flow area A_t ā Area vector C_D Drag coefficient $\overline{C_D}$ Mean drag coefficient Calibration coefficient for DES C_{DES} C_L Lift coefficient $\overline{C_L}$ Mean lift coefficient Drift Coefficient C_{Df} C_p Pressure coefficients d The wall distance D_l Mesh Domain length dt^* Non-dimensional time step Resultant of body forces f_b Elevating function f_e Damping function f_{v1} Damping function depending on the IDDES formulation f_{Δ} G Height of the gap beneath the model G/h Ground clearance ratio h Height of the notchback Ahmed body model I Identity tensor K Kurtosis k Turbulent kinetic energy Turbulence length scale l_k IDDES length scale l_{IDDES}

 L_r Reattachment length L_R Recirculation length p Mean static pressure

p Spatial filtered pressure

 \hat{p} RANS averaged and LES filtered combined pressure

 p_{∞} Freestream atmospheric pressure

 P_{uu} Streamwise component of turbulence production P_{vv} Wall-normal component of turbulence production

 P_{ww} Spanwise component of turbulence production

 P_k Production of turbulent kinetic energy

R Reynolds stress tensor

Re1E4 $Re_h = 1 \times 10^4$ Re5E4 $Re_h = 5 \times 10^4$ Re Reynolds number

 Re_h Reynolds number based on the height h of model.

S Strain rate tensor from the resolved velocity field

 S_u User-specified source term

 $S_{\tilde{v}}$ Defined source term

T Viscous stress tensor

 T_{RANS} Stress tensor

T_{SGS} Subgrid scale stress tensor

T Spatial filtered tensor

RANS averaged and LES filtered combined viscous stress tensor

 U_{∞} Freestream/Characteristic velocity scale

u Instantaneous streamwise velocity

 U_r^b Maximum backflow velocity over the slant

 U_R^b Maximum backflow velocity behind the back

V Mean wall-normal velocity

v Instantaneous wall-normal velocity

V Control volume

 \bar{v} Mean velocity

v Spatial filtered velocity

v RANS averaged and LES filtered combined velocities

v' Fluctuating velocity

v Instantaneous velocity

 V_l C-pillar vortices from the left

 V_r C-pillar vortices from the right

 V_c Vortices associated with the shear layer from the roof

 y_g^+ Maximum wall y+ on the ground of the mesh domain

 y_b^+ Maximum wall y+ on the body of the notchback Ahmed body

 $\overline{u'u'}$ Streamwise Reynolds normal stress

 $\overline{u'v'}$ Streamwise – Wall-normal Reynolds shear stress

 $\overline{v'v'}$ Wall-normal Reynolds normal stress

 $\overline{w'w'}$ Spanwise Reynolds normal stress

 $\overline{u'w'}$ Streamwise – Spanwise Reynolds shear stress

W Mean spanwise velocity

w Instantaneous spanwise velocity

x Streamwise direction
 y Wall-normal direction
 z Spanwise direction

 α Slant angle

 β_e Effective backlight angle

β Backlight angle

 $\partial U/\partial y$ Mean Shear

 $\Delta C_p h/\Delta z$ Spanwise pressure gradients

 Δt Time step ρ Density

 \tilde{v} Modified diffusivity

 μ_t Turbulent eddy viscosity

 σ Stress tensor

 $\sigma_{\tilde{v}}$ Model coefficient

 ϕ Solution variable

 $\tilde{\phi}$ Filtered value

 ϕ' Sub-grid value

 Δ_{IDDES} Locally determined grid spacing

Δ Local grid size

 Δ_{min} Smallest distance between a cell center and its neighbors

Chapter 1

Introduction

1.2 Motivation

Transportation is a major contributor to greenhouse gas (GHG) emissions, with ground vehicles accounting for about 75% of transportation-related emissions (Ritchie & Roser, 2024). Reducing GHG emissions through electrification requires an improved understanding of vehicle aerodynamics to optimize battery efficiency and increase the driving range of green vehicles.

In the flow around a ground vehicle, shown in figure 1.1(a), a wake is created at the back of the vehicle, which is a region of lower pressure than at the front. The difference in pressure at the leading edge and rear edge of the vehicle creates a force that acts in the direction of the flow. If the vehicle moves forward, which is in the direction opposite to the flow, this force, forming part of the total drag called the pressure drag, will oppose the vehicle's motion, requiring more energy to overcome it. Hence, this necessitates the need to study flow motions in the wake in order to control it.

The flow around ground vehicles is studied with the use of simple vehicle models, which include Ahmed Body (Ahmed et al., 1984), DrivAer model (Wieser et al., 2020) and Windsor body (Pavia et al., 2018). The standard Ahmed body (see figure 1(b)), also known as fastback, as the name hints, was first used by Ahmed et al. (1984) to study the wake structure of the flow around it by varying the rear end slant angle and linking the results to ground vehicles (e.g. Sport Utility Vehicles (SUVs)). Their work has led to increased interest in the use of Ahmed Body models to replicate wake flow around ground vehicles. A remarkable contribution from this work is that Ahmed et al. (1984) reported that 85% of the Ahmed body's drag is made of pressure drag, with

most of it generated from the rear part of the body. This is one of the key reasons why the wake structure is of major interest in studies that aim to replicate the wake flow of ground vehicles under a wide range of geometric and flow conditions. The other variations of the Ahmed body aside the fastback based on the geometrical shape of their rear end are the squareback Ahmed body (see figure 1(c)) (Grandemange et al., 2012a) and notchback Ahmed body (see figure 1(d)) (Sims-Williams et al., 2011; He et al., 2021a; He et al., 2021b) which are used for mimicking the wake behind trucks and sedan passenger vehicles, respectively. All rear-end variations of the Ahmed body share a common front and midsection design, intended to produce a strong three-dimensional and relatively uniform flow, ultimately generating a large wake at the rear end (Ahmed et al., 1984). Studies conducted on Ahmed body models have focused mostly on the wake characteristics of the fastback and squareback rear end geometries. However, the notchback is not well understood despite its more complex wake structure due to the trunk at the rear-end.

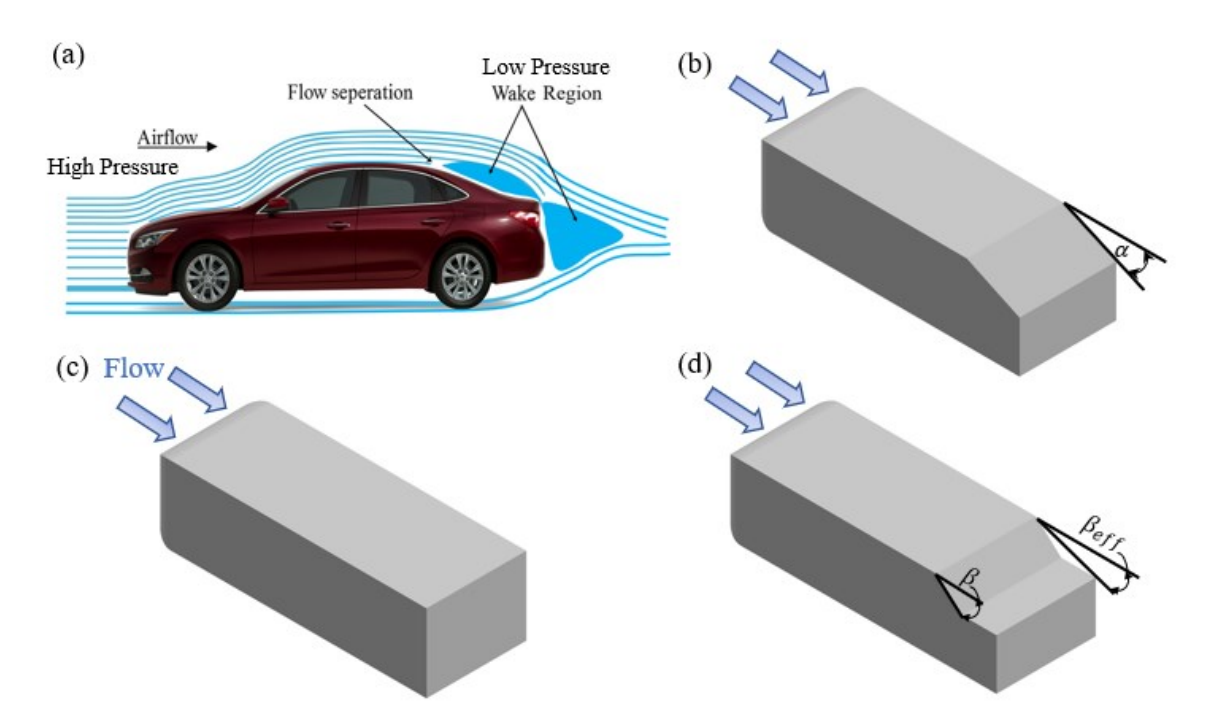


Figure 1.1 Representation of (a) flow around a ground vehicle (b) hatchback, (c) square-back, and (d) notchback Ahmed body with the nomenclature.

1.2 Literature review

1.2.1 Salient Flow Features of The Ahmed Body Wake

Ahmed et al. (1984) investigated the time-averaged flow structures in the wake of the fastback Ahmed body, highlighting some salient flow features. The salient flow features of the fastback (see figure 1.2) consist of a separation bubble on the slanted surface, recirculation bubbles behind the vertical base and a pair of counterrotating longitudinal vortices generated from the sides of the rear end called C-pillar vortices. These structures are formed due to flow separation, vortex shedding and multiple shear layer interactions in the wake. Flow separation around an Ahmed body refers to the separation of the boundary layer from the surface of a body, leading to the formation of a recirculation region. For the fastback model, a recirculation region, also known as a separation bubble, is formed on the slant due to flow separation from the trailing edge of the roof and reattachment. Behind the vertical base, two recirculation bubbles are formed due to separated flows from the trailing edge of the slant and the bottom of the base.

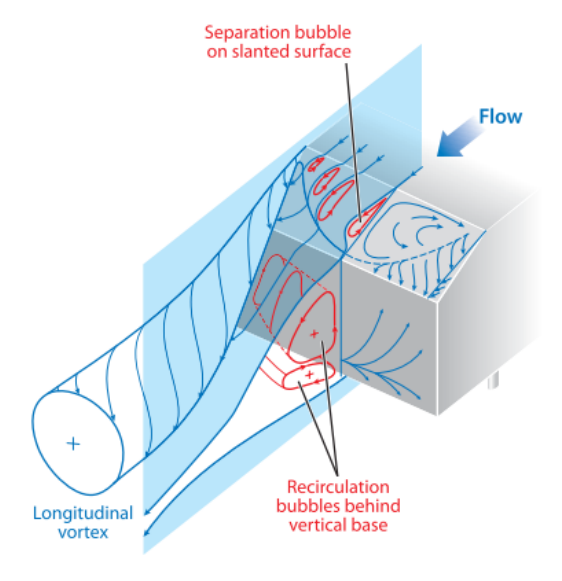


Figure 1.2 Time-averaged three-dimensional flow structures in the wake redrawn from (Ahmed et al., 1984) by Choi et al. (2014).

These flow structures are unsteady and three-dimensional, and their generation and strength are known to influence the aerodynamics of the model.

1.2.2 Geometric and Flow Parameters Influencing the Wake Dynamics

The flow around ground vehicle models (i.e. Ahmed body) is studied using both experimental techniques and numerical simulations. The experimental techniques include hotwire anemometry (Kohri et al., 2014), laser doppler velocimetry (Tunay et al., 2013), time resolved planar particle image velocimetry (TR-PIV, 2D-2C) (Siddiqui & Agelin-Chaab, 2022), stereoscopic (Stereo) PIV (2D, 3C) (Ladwig et al., 2023) and volumetric/tomographic (tomo) PIV (Chen et al., 2024). The numerical simulations include Direct Numerical Simulations (DNS) (Prakash et al., 2018), RANS-based models (Ouedraogo & Essel, 2024) and Scale Resolving methods such as improved delayed detached eddy simulations (IDDES) (Guilmineau, 2018; Kang et al., 2021).

Both experimental and numerical studies have demonstrated that the wakes of the various types of Ahmed bodies are influenced by their geometric parameters and the approach flow conditions upstream of the models. The geometric parameters include the slant angle (α) f or a fastback (Ahmed et al., 1984; Strachan et al., 2007; Vino et al., 2005), backlight (β) and effective backlight (β_e) angles for the notchback Ahmed body (Sims-Williams et al., 2011) and the aspect ratios (h/W) or (h/W) or (h/W) where (h/W) are the height, length and width of the model Grandemange et al., (2013a). Also, the ground clearance ratio (G/h) where (G/h) is the height of the gap beneath the model Grandemange et al., (2013a), blockage ratio defined as the ratio of frontal area of the model to cross-sectional area of the flow (He et al., 2021c) and the model surface roughness influence the wake characteristics. The approach flow conditions affecting the wake features include the Reynolds number (Grandemange et al., 2012a; Ouedraogo & Essel, 2024),

crosswinds/yaw angle (Bello-Millán et al., 2016), freestream turbulence intensity (Chen et al., 2023; Passaggia et al., 2021) and the relative boundary layer thickness (Kang et al., 2021).

For the rear-end geometry, the slant angle (α) for a fastback when varied, has been shown to influence the strength of the C-pillar vortices, the recirculation bubbles at the back and the mean drag coefficient of the model (Ahmed et al., 1984; Strachan et al., 2007; Vino et al., 2005). The slant angle $\alpha = 30^{\circ}$ was identified as critical angle for the highest drag coefficient. Based on this angle α , the wake structure changes, for instance, Strachan et al., (2007) reported that at values $(\alpha \le 12.5^{\circ})$, the separated flow from the trailing edge of the roof fully attaches to the slant with a weak pair of longitudinal vortices in the near wake region, resulting in a mean aerodynamic drag coefficient $\overline{C_D} \approx 0.25$. For values of $12.5^{\circ} < \alpha \le 30^{\circ}$, the longitudinal vortices are stronger and the mean drag coefficient increases with slant angle Vino et al. (2005). For values $\alpha > 30^{\circ}$, the flow fully separates over the slant associated with significantly weak C-pillar vortices and very low drag. Krajnović & Davidson (2005) using large eddy simulation (LES), observed additional pair of counter-rotating vortices generated near the bottom corners of the base for $\alpha = 25^{\circ}$. When the fastback with the same slant angle is modified by rounding the sides of the trailing end known as the elliptical Ahmed body, it reoriented the recirculation bubbles and shifted the high-drag regime of the standard Ahmed body to a low-drag regime (Siddiqui & Agelin-Chaab, 2022). When the slant angle of a fastback is changed to $\alpha = 90^{\circ}$, a square back Ahmed body is obtained. In contrast to the fastback Ahmed body, the square-back Ahmed body has only recirculation bubbles behind the vertical base of the body, yet its wake dynamics is complex mainly due to vortex shedding.

On the influence of the aspect ratios (h/W or L/W) and ground clearance ratio (G/h), investigations by Grandemange et al., (2013a) demonstrated that the bi-modality feature of the

squareback is dependent on the ground clearance and the aspect ratio (h/W) of the model. Bi-modality is characterized by random shift of the reverse flow region between two reflectional symmetry-breaking (RSB) or asymmetric wake positions caused by the instabilities in the shear layers (Grandemange et al., 2012). For low values of ground clearance, G/h < 0.07, only one recirculation bubble is formed behind the back of the body due to the viscous effects on the ground and no sign of bi-modality was observed. As the ground clearance ratio rises into the moderate range of $0.07 \le G/h < 0.12$, the viscous effects gradually diminish, and the flow become more energetic and exits the gap as jet-like upwash flow forming two recirculation bubbles when it interacts with downwash from the roof. For high ground clearance ratios (G/h > 0.12), the flow separation on the ground is suppressed due to a more energetic upwash from the underbody. A pair of recirculation bubbles is formed behind the back, which is associated with the torus (Krajnović & Davidson, 2004; Lucas et al., 2017). At higher ground clearance ratios of $G/h \ge 0.7$, the bimodality phenomenon is present.

The approach flow conditions such as the Reynolds number, crosswinds/yaw angle, freestream turbulence intensity and Relative boundary layer thickness has been widely explored for the fastback and squareback (Bello-Millán et al., 2016; Fan et al., 2020; Passaggia et al., 2021). Reynolds number study by Grandemange et al. (2012) documented and characterized the bi-modal wake behaviour observed on the square-back Ahmed body and reported that the bi-modality behaviour appeared after a critical Reynolds number of $Re \sim 365$ in the laminar regime. However, the bi-modality is found to be independent of the Reynolds number in the turbulent regime, up to $Re = 2.5 \times 10^6$ (Fan et al., 2020). Investigations by Bonnavion & Cadot (2018) and Haffner et al (2020) also demonstrate a suppression of the bi-modality due to yaw and pitch angle. The bi-modality is found to have timescales of approximately $1000h/U_{\infty}$, where h is the height of the

body and U_{∞} is the freestream velocity and is characterized by random shift of the reverse flow region between two reflectional symmetry-breaking (RSB) positions (Volpe et al., 2015).

1.2.3 Notchback Ahmed body

This review focuses on the notchback Ahmed body, as its wake dynamics remain less well understood compared to other Ahmed body rear-end configurations. The notchback model features a rear-end geometry that resembles the rear end shape of a three-box sedan passenger vehicle, as mentioned in the introduction, which is a commonly used ground vehicle. Due to its distinct rearend geometry, the wake of the notchback Ahmed body has specific wake characteristics which differ from those of both the squareback and the fastback rear-end geometries. For the notchback, the separated flow from the roof may attach onto the deck of the trunk or shed directly into the wake behind the vertical base, depending on the backlight angle β and the effective backlight angle β_e (He et al., 2021a; Sims-Williams et al., 2011). The backlight angle β is defined as the inclination angle of the slant, while β_e represents the angle formed by a straight line connecting the trailing edges of the roof and the deck (see Figure.1). Notchbacks exhibit a maximum drag (at $\beta_e = 42$) when the time-averaged flow separates over the backlight but reattaches just before the rear of the model associated with strong trailing vortices from the c-pillars (Sims-Williams et al., 2011). The vortices shed in the spanwise and streamwise direction contribute to the unsteadiness in the wake. These vortices are visualized using various methods, including vorticity contours in 2D planes, iso-surfaces of the Q-criterion (Hunt et al., 1988), iso-surfaces of mean pressure (Fan et al., 2020; He et al., 2021), and proper orthogonal decomposition (Chen et al., 2024; He et al., 2021a).

Sims-Williams et al. (2011) investigated the effects of β (17.8° – 90°) and β_e (17.8° – 31.8°) angles on the time averaged wake structure of notchback configurations at $Re_h = 50000$. The experiments were conducted using surface flow visualization, standard

particle image velocimetry (PIV) and were augmented by 3D numerical simulations using unsteady Reynolds-averaged Navier–Stokes (URANS). Two main flow regimes were identified based on β_e : reattached flow ($\beta_e < 25.3^\circ$) on the deck and fully separated flow ($\beta_e > 25.3^\circ$). Sims-Williams et al. (2011) also found that within the reattached flow regime, the notchback geometries exhibit a symmetric wake topology at $\beta_e = 21.0^\circ$ and an asymmetric wake structure at $\beta_e = 17.8^\circ$. This work further highlights the dependence of aerodynamic drag on the varying β_e angles. The asymmetric wake structure has also been observed in previous flow visualization studies of a notchback car by Cogotti (Cogotti, 1986).

He et al. (2021) conducted large eddy simulation (LES) of the unsteady wake dynamics of the notchback at $\beta_e=17.8^\circ$ and $\beta_e=21.0^\circ$ based on the experiments of Sims-Williams et al. (2011). The asymmetric case ($\beta_e = 17.8^{\circ}$) exhibited a stochastic wake bimodality with large timescales, like bimodality observed behind squareback models (Grandemange et al., 2013a). The asymmetry of the wake was attributed to asymmetric separation from the roof of the body and the associated asymmetric reattachment on the deck. He et al. (2021c) investigated the effects of blockage ratio, $BR \in [0, 20]$ on the bimodality of the notchback ($\beta_e = 17.8^{\circ}$) and found that the wake becomes symmetric when BR > 10. In He et al. (2021b), rounding the trailing edge of the roof was also observed to suppress wake bimodality. He et al. (2021b) further examined the effects of high $Re_h(5 \times 10^4, 10 \times 10^4, 250 \times 10^4)$ on the asymmetric state of the notchback ($\beta_e = 17.8^\circ$) using LES and wind tunnel experiments (pressure taps and hot wire measurements). At $Re_h = 5 \times 10^4$, the wake exhibited bimodality, but as the Reynolds number increased, it transitioned into a tri-stable state, due to the emergence of an additional symmetric wake state. He et al. (2022) demonstrated that floor motion, mimicking on road conditions of vehicles has negligible impact on the degree of wake asymmetry. Recently, Ouedraogo & Essel, (2024) conducted an extensive numerical study on the effects of low-Reynolds number $(0.5 \times 10^4 \le Re_h \le 5 \times 10^4)$ on a notchback $\beta_e = 17.8^\circ$ using RANS. The results categorized the wake structure into symmetric $(Re_h \le 1 \times 10^4)$, transitional $(1 \times 10^4 < Re_h \le 3.5 \times 10^4)$, and fully asymmetric $(Re_h > 3.5 \times 10^4)$ states, demonstrating the sensitivity of wake asymmetry and other time-averaged wake characteristics to Reynolds number.

1.3 Objective

Although prior studies by Ouedraogo & Essel (2024) and He et al. (2021b) has provided valuable insights into the wake regimes of the notchback with $\beta_e = 17.8^{\circ}$ at $Re_h \leq 5 \times 10^4$ and $Re_h \geq 5 \times 10^4$, respectively, the unsteady wake dynamics governing the symmetric and asymmetric flow regimes at lower Reynolds numbers ($Re_h \leq 5 \times 10^4$) are still not fully characterized. To address this gap, the present study aims to investigate the influence of Reynolds number ($Re_h = 1 \times 10^4$ (symmetric regime) and $Re_h = 5 \times 10^4$ (fully asymmetric regime)) on the unsteady wake characteristics of the notchback Ahmed body with $\beta_e = 17.8^{\circ}$ using three-dimensional improved delayed detached eddy simulations (IDDES). The IDDES numerical modeling approach has been previously applied to unsteady flow simulations around Ahmed bodies and has shown good agreement with experimental data (Fan et al., 2020; He et al., 2021d; Kang et al., 2021). The study investigates salient features of the wake for the two contrasting flow regimes, including the turbulent structure, large-scale anisotropy, the pumping motion of recirculation bubbles, and the global dynamic modes.

1.4 Organisation

The thesis comprises four chapters, each summarized as follows:

Chapter 1 provides a general introduction, highlighting the motivation behind the thesis and giving a brief literature review on the wake dynamics of the different types of Ahmed body. It also outlines the research objectives and the structure of the thesis.

Chapter 2 introduces the governing equations relevant to computational fluid dynamics (CFD) simulations, along with a brief overview of the turbulence models employed in this study.

Chapter 3 is adapted from a research paper currently under review in the International Journal of Heat and Fluid Flow. I am the lead author of the paper, which is co-authored by my colleagues Adime K. Bonsi, Newton F. Ouedraogo and my supervisor, Ebenezer Ekow Essel. I performed the simulations, analyzed the data, and wrote the manuscript. My co-authors provided valuable feedback and assisted with the interpretation of the results and the evaluation of the manuscript. The chapter consists of the following subsections as part of the paper: 3.1 Introduction, 3.2 Numerical Setup and Methodology and 3.3 Results and Discussions. The study investigates the influence of Reynolds number on the unsteady turbulent wake regimes of a notchback Ahmed body with an effective backlight angle of 17.8°. Detailed aspects of the wake dynamics, including the mean flow, Reynolds stresses, large-scale anisotropy, global instabilities, and the pumping motion (i.e., quasi-periodic expansion and contraction) of reverse flow regions, are used to characterize the effects of Reynolds number.

Chapter 4 presents the conclusion, summarizing the main findings and insights gained from the study. Additionally, it provides recommendations for future research in this area.

Chapter 2

This chapter introduces the principles of mass and momentum conservation. It also provides a brief overview of the turbulence models used in this study, with comprehensive details available in the STAR-CCM+ User Guide (Siemens Digital Industries Software, 2020).

Methodology

2.1 Governing equations

2.1.1 Conservation of mass

The law of conservation of mass simply relates the total mass of fluid entering and leaving a control volume to the net mass within the control volume during a time interval Δt . This is shown in the equation below. The continuity equation is derived from the law of conservation of mass for a control volume and simplified as shown below.

Continuity

$$\frac{\partial}{\partial t} \int_{\mathbf{V}} \rho \ d\mathbf{V} + \oint_{A} \rho \mathbf{v} \cdot d\mathbf{a} = \int_{\mathbf{V}} S_{u} \ d\mathbf{V}$$
 (2.1)

where:

t is time, V is volume, a is the area vector, ρ is the density, A is the surface area, v is the velocity vector and S_u is a user-specified source term.

$$\frac{\partial \rho}{\partial t} + \nabla \cdot (\rho \mathbf{v}) = 0 \tag{2.2}$$

2.1.2 Conservation of momentum

The momentum of a system remains constant when the net force acting on it is zero, and thus the momentum of such systems is conserved. This is known as the law of conservation of momentum. They account for the effect of pressure, viscous forces, and gravity on the fluid motion.

$$\frac{\partial}{\partial t} \int_{V} \rho \mathbf{v} \, d\mathbf{V} + \oint_{A} \rho \, \mathbf{v} \otimes \mathbf{v} \cdot d\vec{\mathbf{a}} = -\oint_{A} p \, \mathbf{I} \cdot d\vec{\mathbf{a}} + \oint_{A} \mathbf{T} \cdot d\vec{\mathbf{a}} + \int_{V} \mathbf{f}_{\mathbf{b}} \, d\mathbf{V} + \int_{V} S_{u} \, d\mathbf{V}$$
 (2.3)

where:

p is pressure, T is the viscous stress tensor, f_b is the resultant of body forces (such as gravity and centrifugal forces) per unit volume acting on the continuum), \otimes denotes the outer product, and S_u is a user-specified source term.

$$\frac{\partial}{\partial t}(\rho \mathbf{v}) + \nabla \cdot (\rho \mathbf{v} \otimes \mathbf{v}) = -\nabla \cdot p\mathbf{I} + \nabla \cdot (\mathbf{T}) + \mathbf{f_b}$$
(2.4)

For a fluid, the stress tensor is often written as sum of normal stresses and shear stresses,

$$\sigma = -pI + T \tag{2.5}$$

The Navier-Stokes equation is the combination of the continuity equation and the momentum equations, which are treated as a system of four equations to be solved.

2.2 Turbulence modelling

2.2.1 Introduction

Turbulence is defined as a state of fluid motion characterized by chaotic, irregular fluctuations in velocity and other flow properties. These fluctuations span a wide range of spatial and temporal scales and are inherently unsteady. The largest scales are determined by the flow domain (geometry) and the small scales are determined by the fluid viscosity and they depend on Reynolds number (Re). The Reynolds number is the ratio of inertia forces (nonlinear) to the linear viscous force which is usually formulated as $Re = U_{\infty}L/\nu$, where L is the characteristic length scale, U_{∞} is a characteristic velocity scale and v is kinematic viscosity. The inertial forces are responsible for the flow instability while the viscous forces convert the kinetic energy into thermal energy. The smallest length scale is called the Kolmogorov length scale, $l = (v^3L/U_{\infty}^3)^{1/4}$. Turbulent flows are governed by the Navier-Stoke equations. Since the equations are highly non-linear, non-integrable and non-local, they are difficult to solve and hence are modelled through computational methods such as direct numerical simulation (DNS). In many engineering applications, resolving all the scales or turbulent structures directly through time-resolved simulations known as the DNS is computationally expensive due to the fine resolution required especially at high Re.

Therefore, other turbulence models that are computationally less expensive to DNS are mostly implemented in modelling or resolving some scales in flows. These are the Reynolds-Averaged Navier-Stokes (RANS) turbulence models and Scale-resolving simulations. It is generally understood that turbulence models are simplified representations of complex physical phenomena. Their performance varies with flow type and boundary conditions, and identifying conditions under which a given model performs well or poorly is typically informed by accumulated experience and validation studies.

2.2.2 Reynolds Averaged Navier-Stokes equations

The Reynolds-Averaged Navier-Stokes equations are obtained by decomposing, each solution variable (i.e. velocity, pressure) in the instantaneous Navier-Stokes equations into its mean or averaged value and its fluctuating component. For instance, the instantaneous velocity vector v should be decomposed as $v = \bar{v} + v'$, where \bar{v} represents mean velocity and v' is the fluctuating component. The averaging can be time-averaging for steady-state situations and ensemble averaging for repeatable transient situations. Inserting the decomposed solution variables into the Navier-Stokes equations results in the equations below:

Mean mass

$$\frac{\partial \rho}{\partial t} + \nabla \cdot (\rho \overline{\mathbf{v}}) = 0 \tag{2.5}$$

Mean momentum

$$\frac{\partial}{\partial t}(\rho \overline{\mathbf{v}}) + \nabla \cdot (\rho \overline{\mathbf{v}} \otimes \overline{\mathbf{v}}) = -\nabla \cdot \overline{p}\mathbf{I} + \nabla \cdot (\overline{\mathbf{T}} + \mathbf{T}_{RANS}) + \mathbf{f}_{b}$$
 (2.6)

where:

 ρ is the density, \overline{v} is the mean velocity, \overline{p} is the mean pressure, \overline{T} is the mean viscous stress tensor, f_b is the resultant of the body forces (such as gravity and centrifugal forces) and the RANS stress tensor,

$$T_{RANS} = -\rho R + \frac{2}{3}\rho kI \tag{2.7}$$

$$R = \begin{pmatrix} \frac{\overline{u'u'}}{\underline{u'v'}} & \frac{\overline{u'v'}}{\underline{v'v'}} & \frac{\overline{u'w'}}{\underline{v'w'}} \\ \frac{\overline{u'w'}}{\underline{v'w'}} & \frac{\overline{v'v'}}{\underline{v'w'}} & \frac{\overline{w'w'}}{\underline{w'w'}} \end{pmatrix}$$
(2.8)

where k is the turbulent kinetic energy and R is the Reynolds stress tensor. The challenge is thus to model T_{RANS} in terms of the mean flow quantities, and hence provide closure of the governing equations. Two basic approaches used are the Eddy viscosity models and Reynolds stress transport models. The Eddy viscosity models are based on the Boussinesq Eddy Viscosity Assumption which proposed that the Reynolds stresses are proportional to the mean rates of deformation. Examples include the mixing length and the Spalart Allmaras models. The Reynolds stress transport models are based on solving the transport equations of the Reynolds stresses. An example is the Launder, Reece and Rodi – Isotropization of Production (LRR-IP) model (Launder et al., 1975). The following section focuses on the standard Spalart-Allmaras model, which was selected as the RANS part of the turbulence model used in the present study.

2.2.2.1 Standard Spalart Allmaras (SSA) model

The Spalart-Allmaras turbulence model is an Eddy viscosity model that solves a transport equation for the modified diffusivity \tilde{v} in order to determine the turbulent eddy viscosity (Spalart & Allmaras, 1992).

The turbulent eddy viscosity μ_t is calculated as:

$$\mu_t = \rho f_{v1} \tilde{v} \tag{2.9}$$

and the transport equation for \tilde{v} is

$$\frac{\partial}{\partial t}(\rho \tilde{v}) + \nabla \cdot (\rho \tilde{v} \bar{v}) = \frac{1}{\sigma_{\tilde{v}}} \nabla \cdot [(\mu + \rho \tilde{v}) \nabla \tilde{v}] + P_{\tilde{v}} + S_{\tilde{v}}$$
(2.10)

where f_{v1} , $\sigma_{\tilde{v}}$, $P_{\tilde{v}}$, and $S_{\tilde{v}}$ are the damping function, the model coefficient, the production term and user defined source term, respectively.

2.2.3 Scale-Resolving Simulations

In contrast to RANS models, scale-resolving simulations resolve the large scales of turbulence and model small-scale motions. Two approaches are commonly used, which are the Large Eddy Simulations (LES) and Detached Eddy Simulations (DES).

2.2.3.1 Large Eddy Simulations (LES)

A Large Eddy Simulation (LES) is a transient technique in which the large scales of the turbulence are directly resolved everywhere in the flow domain, and the small-scale motions are modeled (Pope, 2000). LES resolves turbulent structures in space everywhere in the flow domain down to the grid limit, where subgrid models approximate the impact of the subgrid structures on the flow field (Smagorinsky, 1963). In order to resolve the crucial turbulent structures near the wall, this approach requires an excessively high mesh resolution in the wall boundary layer, not only in the direction normal to the wall but also in the flow direction (Pope, 2000; Piomelli, 1999). One rationale behind using the LES technique is that, by directly resolving a greater portion of the turbulent flow and modeling only the smaller scales, the impact of assumptions made in turbulence modeling becomes less significant. The downside of the approach is the computational expense, which, although less than direct numerical simulation, is still nonetheless excessive (Pope, 2000).

In contrast to the RANS equations, the equations that are solved for LES are obtained by a spatial filtering rather than an averaging process. Each solution variable ϕ is decomposed into a filtered value $\tilde{\phi}$ and a sub-filtered, or sub-grid, value ϕ' :

$$\phi = \tilde{\phi} + \phi' \tag{2.11}$$

where ϕ represents velocity components, pressure, energy, or species concentration.

The spatial filtering removes the smaller eddies, associated with higher frequencies and thereby reduces the range of scales that must be resolved. LES filtering can be either explicit or implicit. Explicit filtering applies a filter function (such as box or Gaussian) to the discretized Navier-Stokes equations. The filtered velocity is obtained by using a filter function, say G(r) (Leonard, 1975). The filtering of the generic instantaneous flow variable $\phi(t, x)$ is defined as:

$$\tilde{\phi}(t,x) = \iiint_{-\infty}^{\infty} G(x - x', \Delta) + \phi(t, x') dx'$$
(2.12)

where $G(x, \Delta)$ is the filter function characterized by a filter width $\Delta = (\Delta_x \Delta_y \Delta_z)^{1/3}$. Inserting the decomposed solution variables into the Navier-Stokes equations results in equations for the filtered quantities defined: The filtered mass and momentum.

$$\frac{\partial \rho}{\partial t} + \nabla \cdot (\rho \tilde{\mathbf{v}}) = 0 \tag{2.13}$$

$$\frac{\partial}{\partial t}(\rho \tilde{\mathbf{v}}) + \nabla \cdot (\rho \tilde{\mathbf{v}} \otimes \tilde{\mathbf{v}}) = -\nabla \cdot \tilde{p}\mathbf{I} + \nabla \cdot (\tilde{\mathbf{T}} + \mathbf{T}_{sgs}) + \mathbf{f}_{b}$$
(2.14)

where: $\tilde{\mathbf{v}}$ is the filtered velocity. \tilde{p} is the filtered pressure, I is the identity tensor. $\tilde{\mathbf{T}}$ is the filtered stress tensor. \mathbf{f}_b is the resultant of the body forces (such as gravity and centrifugal forces). The filtered equations are rearranged into a form that looks identical to the unsteady RANS (equation 2.5 and 2.6). However, the turbulent stress tensor now represents the subgrid-scale stresses. These stresses result from the interaction between the larger, resolved eddies and the smaller, unresolved eddies and are modelled using the Boussinesq approximation as follows:

$$T_{SGS} = 2 (\mu_t) S - \frac{2}{3} (\mu_t \nabla \cdot \tilde{v}) I$$
 (2.15)

where T_{SGS} is the subgrid scale stress tensor, S is the strain rate tensor given and computed from the resolved velocity field \tilde{v} .

The subgrid scale turbulent viscosity μ_t must be described by a subgrid scale model that accounts for the effects of small eddies on the resolved flow. Three subgrid scale models are commonly used, which are the Smagorinsky Subgrid Scale model, Dynamic Smagorinsky Subgrid Scale model and Wall-Adapting Local-Eddy Viscosity (WALE) Subgrid Scale model.

2.2.3.2 Detached Eddy Simulations (DES)

Detached Eddy Simulation (DES) is a hybrid approach that blends RANS and LES methods. It uses RANS near walls and LES in separated, unsteady regions (Spalart, 1997). This allows DES to capture large-scale turbulent structures in the core flow without the high computational cost of wall-resolved LES (Spalart, 1997). However, its accuracy depends on the separation of turbulence and mean-flow time scales, and may be limited by the turbulence model itself (Menter et al, 2002).

DES models apply a RANS formulation in attached boundary layers and switch to LES in detached regions when the grid resolution permits. This provides the benefits of both models, that is, computational efficiency near walls and detailed turbulence resolution in separated zones (Spalart, 1997). Simcenter STAR-CCM+ provides the DES modeling approach for three different RANS models including Spalart-Allmaras DES, Elliptic Blending DES and SST K-Omega DES. It also offers the DES variants, Delayed Detached Eddy Simulation (DDES) and Improved Delayed Detached Eddy Simulation (IDDES). The DDES model introduces a delay function which includes the molecular and turbulent viscosity information to better differentiate between LES and RANS regions. DDES is critical for meshes where spatial refinement could give rise to ambiguous behavior (Spalart et. al, 2006). For IDDES, the subgrid length-scale includes a dependence on the wall distance. This approach allows RANS to be used in a much thinner near-wall region, in which the wall distance is much smaller than the boundary-layer thickness (Spalart et al., 2006).

2.2.3.2.1 Improved Delayed Detached Eddy Simulations (IDDES)

IDDES is a hybrid Reynolds-Averaged Navier-Stokes (RANS)-LES approach that implicitly divides the computational domain into two regions based on a blending function that apply RANS to model the near-wall boundary layers and LES is to resolve the unsteady flow dynamics away from the wall (Germano et al., 1991). IDDES offers a more reliable scale-resolving method for complex flow simulations by reducing grid-induced separation, which is a common issue in delayed detached eddy simulation (DDES) and detached eddy simulation (DES) due to improper LES activation near walls (Spalart, 1997; Spalart et al., 2006). The IDDES model was for the numerical simulations in Star-CCM+ version 2020. IDDES and Star-CCM+ have been used in previous studies of unsteady flow around Ahmed bodies and well-validated against experimental results (Fan et al., 2020; He et al., 2021d; Kang et al., 2021). The selection of the RANS model part of the IDDES used was based on the turbulence model assessment by Ouedraogo & Essel, (2024). They reported that Standard Spalart Allmaras (SSA) model accurately predicts the asymmetric time-averaged wake topology of the notchback at $Re_h = 5 \times 10^4$. This informed the use of the SSA model as RANS model used in IDDES simulations for the current study. Other RANS models used in the turbulence model assessment did not predict the asymmetric wake topology. These RANS models are the eddy viscosity (EV) models and SMC models. The EV models include two one-equation models: standard Spalart-Allmaras model (denoted as SSA) and high Re Spalart–Allmaras (HRe SA) models, and four two-equation models: realizable k-epsilon two-layer (RKE 2L), V2F k-epsilon (V2F), standard k-omega (SKO) and SST k-omega (SST) models. The SMC models include linear pressure strain two-layer (LPS 2L), quadratic pressure strain (QPS), and elliptic blending (EB) models (Ouedraogo & Essel, 2024). The SSA model also predicted aerodynamic coefficients which were in good agreement with LES

results reported by He et al., (2021d). The momentum equations for IDDES are based on the DES model given as:

$$\frac{\partial}{\partial t}(\rho \hat{\mathbf{v}}) + \nabla \cdot (\rho \hat{\mathbf{v}} \otimes \hat{\mathbf{v}}) = -\nabla \cdot \hat{p}\mathbf{I} + \nabla \cdot (\hat{\mathbf{T}} + \mathbf{T}_{model}) + \mathbf{f}_{b}$$
 (2.16)

where $\hat{\mathbf{v}}$, \mathbf{I} , ρ , \hat{p} , $\hat{\mathbf{T}}$, \mathbf{f}_b represent the RANS averaged and LES filtered combined velocities, identity tensor, density, pressure, viscous stress tensor and body forces, respectively. The modeled stress tensor, \mathbf{T}_{model} , for IDDES which is a variant of the DES model is expressed as:

$$T_{model} = f_{\Delta} \left(\frac{\Delta}{l_k}\right) T_{RANS} \tag{2.17}$$

where f_{Δ} is a damping function depending on the IDDES formulation, and l_k is the turbulence length scale.

 T_{RANS} is evaluated as

$$T_{RANS} = 2\mu_t S - \frac{2}{3} \langle \mu_t (\nabla \cdot \overline{\nu}) \rangle I$$
 (2.18)

where S, is the mean strain rate tensor. The SSA solves one transport equation for the modified diffusivity \tilde{v} and turbulence eddy viscosity μ_t , computed as

$$\mu_t = \rho f_{v1} \tilde{v} \tag{2.19}$$

where f_{v1} is a damping function. The IDDES length scale, l_{IDDES} which governs the switching between RANS and LES regions, is defined as (Shur et al., 2008):

$$l_{IDDES} = \tilde{f}_d (1 + f_e) l_{RANS} + (1 - \tilde{f}_d) C_{DES} \Delta_{IDDES}$$
 (2.20)

$$l_{les} = C_{DES} \Delta_{IDDES} \tag{2.21}$$

where \tilde{f}_d is a shielding function that controls the transition between RANS and LES, f_e is an elevating function for wall-modeled LES (WMLES) regions, l_{RANS} is the RANS length scale, C_{DES} is a calibration coefficient, and Δ_{IDDES} is the locally determined grid spacing given by:

$$\Delta_{IDDES} = min(max(0.15d, 0.15\Delta, \Delta_{min}), \Delta)$$
 (2.22)

where d is the wall distance, Δ is the local grid size, and Δ_{min} is the smallest distance between a cell center and its neighbors. This formulation ensures the model dynamically transitions between RANS near walls, LES in separated and free-shear regions, and WMLES in regions with sufficient resolution thereby reducing Reynolds number dependency (Shur et al., 2008). Further details of the formulations can be found in the Simcenter Star-CCM+ version 2020 User Guide (Siemens Digital Industries Software, 2020).

Chapter 3

This chapter is based on the work of Kodie-Ampaw et al., (2025), which investigates the influence of Reynolds number on the unsteady turbulent wake regimes of a notchback Ahmed body with an effective backlight angle of 17.8°. Three-dimensional improved delayed detached eddy simulations (IDDES) were conducted at two Reynolds numbers. Detailed aspects of the wake dynamics, including the mean flow, Reynolds stresses, large-scale anisotropy, global instabilities, and the pumping motion (i.e., quasi-periodic expansion and contraction) of reverse flow regions, are used to characterize the effects of Reynolds number.

3.1 Introduction

Flow around bluff bodies is often used to investigate the aerodynamics of ground vehicles, with the goal of using these insights to develop effective drag reduction strategies. Such strategies are essential for reducing fuel consumption and increasing the driving range of electric vehicles, contributing to global efforts to reduce greenhouse gas (GHG) emissions and mitigate their impact on climate change. The generic Ahmed body (Ahmed et al., 1984) is widely used to study the wake structure behind ground vehicles. The model consists of a fore-end with rounded edges, a rectangular midsection, and a rear-end that can be configured into a squareback to mimic semi-truck trailers and buses, a hatchback for sport utility vehicles (SUVs), or a notchback with a trunk (figure 3.1) for sedans. The wake structure of the Ahmed body is usually characterized by a three-dimensional (3D) vortex system consisting of von Kármán vortex shedding from the trailing edges, counter-rotating longitudinal vortices from the corners, recirculation bubbles undergoing quasi-periodic expansion and contraction (i.e., a pumping motion), and multiple separated shear layers interacting with each other. The instabilities in the shear layers can also induce stochastic wake

asymmetry, exhibiting dynamic modes, e.g., bimodality (Grandemange et al., 2012; He et al., 2021a) or tri-modality (He et al., 2021b). While the 3D vortex system and associated instabilities have been extensively investigated for the hatchback and squareback Ahmed bodies (Ahmed et al., 1984; Grandemange et al., 2012), the unsteady wake structure of the notchback is relatively less well-understood.

The salient flow features of the notchback may include recirculation bubbles near the rounded fore-end and the redevelopment of the boundary layer along the four sides of the mid-section of the body. On the top surface, flow separates from the trailing edge of the roof and may either reattach onto the slant or deck of the trunk or shed directly into the wake behind the vertical back (Sims-Williams et al., 2011; He et al., 2021a). In the case of flow reattachment in the slant-deck region, subsequent separation at the top and bottom trailing edges of the vertical back generates primary counter-rotating recirculation bubbles, associated with strong downwash from the top and upwash from the gap between the body and the wall. Additionally, flow separation from the sides of the trunk leads to the formation of side recirculation bubbles, which, together with the primary bubbles, are footprints of the toroidal structure formed behind the back. Moreover, flow separations from the sides of the slant and their interaction with the flow over the slant generate a pair of counter-rotating longitudinal vortices, often referred to as C-pillar vortices.

Previous studies have shown that the wake characteristics of the notchback depends on important geometric and initial flow parameters such as effective backlight angle (β_e) (He et al., 2021a; Sims-Williams et al., 2011), Reynolds number based on the height (h) of the body and the freestream velocity (U_{∞}), Re_h (He et al., 2021b; Ouedraogo & Essel, 2024), and the geometry

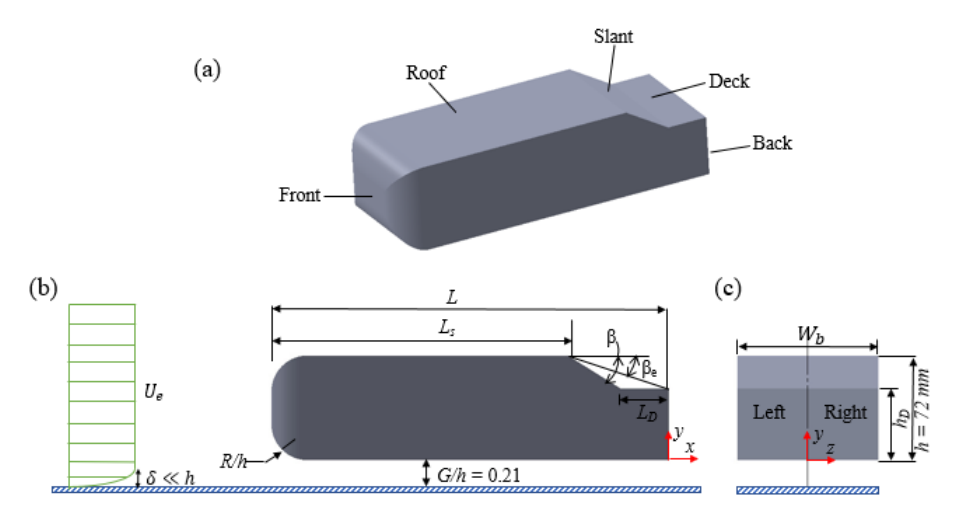


Figure 3.1: Schematic drawing of the notchback Ahmed body with the nomenclature used in the present study.

(sharp/roundness) of the roof trailing edge (He et al., 2021b). As shown in figure 1, the backlight angle (β) is defined as the inclination angle of the slant, while β_e represents the angle formed by a straight line connecting the trailing edges of the roof and the deck. Sims-Williams et al. (2011) investigated the effects of β_e (17.8° – 31.8°) on the wake structure of a notchback at $Re_h = 5 \times 10^4$. The experiments were conducted using surface flow visualization and particle image velocimetry (PIV) in addition to a 3D numerical simulation using unsteady Reynolds-averaged Navier–Stokes (URANS). Two main flow regimes were identified: reattached flow regime ($\beta_e < 25.3^\circ$) and fully separated flow regime ($\beta_e \ge 25.3^\circ$). Sims-Williams et al., (2011) also found that within the reattached flow regime, the notchback geometries exhibit a symmetric wake topology at $\beta_e = 21.0^\circ$ and an asymmetric wake topology at $\beta_e = 17.8^\circ$. The asymmetric wake structure was also reported in previous flow visualization studies of a notchback CNR car model by Cogotti (1986).

He et al. (2021a) conducted large eddy simulations (LES) to investigate the symmetric and asymmetric regimes of the notchback using models with $\beta_e = 17.8^{\circ}$ and 21.0° and at $Re_h = 5 \times 10^4$. The $\beta_e = 17.8^{\circ}$ model depicted an asymmetric wake while the $\beta_e = 21.0^{\circ}$

model exhibited a symmetric wake, in agreement with the experiments of Sims-Williams et al. (2011). However, the asymmetric case ($\beta_e = 17.8^{\circ}$) also displayed a stochastic wake bimodality, with each state persisting over large timescales, similar to the bimodality reported for squareback models (Grandemange et al., 2013a). The wake asymmetry was attributed to asymmetric separation from the roof of the body and the associated asymmetric reattachment on the deck. He et al. (2021c) investigated the effects of blockage ratio, $BR \in [0,20]$ on the bimodality of a notchback ($\beta_e = 17.8^{\circ}$) and found that the wake becomes symmetric for BR > 10. In He et al., 2021b, rounding the trailing edge of the roof was found to suppress wake bimodality. He et al. (2021b) further examined the effects of Re_h (0.5×10^5 , 1×10^5 , 25×10^5) on the asymmetric state of the notchback $\beta_e = 17.8^{\circ}$ using LES and wind tunnel experiments (pressure taps and hot wire measurements). At $Re_h = 5 \times 10^4$, the wake exhibited bimodality, but as the Reynolds number increased, it transitioned into a tri-stable state, due to the emergence of an additional symmetric wake state. He et al. (2022) demonstrated that floor motion, mimicking road conditions of vehicles has negligible impact on the degree of wake asymmetry.

Recently, Ouedraogo & Essel (2024) conducted a numerical study on the effects of low-Reynolds number ($5 \times 10^3 \le Re_h \le 5 \times 10^4$) on the time-averaged wake structure of a notchback with $\beta_e = 17.8^\circ$ using RANS. They found that as the Reynolds number increases, the wake structure transitions through three steady regimes: symmetric ($Re_h \le 1 \times 10^4$), transitional ($1 \times 10^4 < Re_h \le 3.5 \times 10^4$), and fully asymmetric ($Re_h > 3.5 \times 10^4$), demonstrating the sensitivity of wake asymmetry to Reynolds number. The flow asymmetry was attributed to the asymmetric separation of the flow from both the roof trailing edge and C-pillars, which is associated with a strong imbalance in entrainment from the side of the body. They also found that

the mean drag coefficient $(\overline{C_D})$, decreases with increasing Reynolds numbers while the mean lift coefficient $(\overline{C_L})$ is independent of Reynolds number.

While studies by Ouedraogo & Essel (2024) and He et al. (2021b) has provided valuable insights into the wake regimes of the notchback with $\beta_e = 17.8^{\circ}$ at $Re_h \leq 5 \times 10^4$ and $Re_h \geq 5 \times 10^4$, respectively, the unsteady wake dynamics of the symmetric and asymmetric flow regimes at $Re_h \leq 5 \times 10^4$ are still not fully characterized. Therefore, the objective of the present study is to investigate the effects of Reynolds number ($Re_h = 1 \times 10^4$ (symmetric regime) and $Re_h = 5 \times 10^4$ (fully asymmetric regime)) on the unsteady wake characteristics of the notchback Ahmed body with $\beta_e = 17.8^{\circ}$ using 3D improved delayed detached eddy simulations (IDDES). Detailed aspects of the turbulent wake structure, large-scale anisotropy, pumping motion of recirculation bubbles, and the global dynamic modes are examined for the two contrasting flow regimes of the 17.8° notchback Ahmed body. The remainder of this chapter is organized as follows: Section 3.2 describes the numerical setup and methodology; and Section 3.3 presents the results and discussion.

3.2 Numerical Setup

3.2.1 Governing equation of the turbulence model

The three-dimensional unsteady simulations were performed using the IDDES model in Star-CCM+ version 2020. IDDES and Star-CCM+ have been used in previous studies of unsteady flow around Ahmed bodies and well-validated against experimental results (Fan et al., 2020; He et al., 2021d; Kang et al., 2021). IDDES is a hybrid Reynolds-Averaged Navier-Stokes (RANS)-LES approach that implicitly divides the computational domain into two regions based on a blending function that apply RANS to model the near-wall boundary layers and LES is to resolve the

unsteady flow dynamics away from the wall (Germano et al., 1991). The SSA model was chosen as the RANS model used in the IDDES simulations for the present study based on reasons mentioned earlier in section 2.2.3.2.1 of chapter 2. The SSA model is described in section 2.2.2.1 of chapter 2. The IDDES length scale, l_{IDDES} which governs the switching between RANS and LES regions, is defined as (Shur et al., 2008):

$$l_{IDDES} = \tilde{f}_d (1 + f_e) l_{RANS} + (1 - \tilde{f}_d) C_{DES} \Delta_{IDDES}$$
(3.1)

$$l_{les} = C_{DES} \Delta_{IDDES} \tag{3.2}$$

where \tilde{f}_d is a shielding function that controls the transition between RANS and LES, f_e is an elevating function for wall-modeled LES (WMLES) regions, C_{DES} is a calibration coefficient, and Δ_{IDDES} is the locally determined grid spacing given by:

$$\Delta_{IDDES} = min(max(0.15d, 0.15\Delta, \Delta_{min}), \Delta)$$
 (3.3)

where d is the wall distance, Δ is the local grid size, and Δ_{min} is the smallest distance between a cell center and its neighbors. This formulation ensures the model dynamically transitions between RANS near walls, LES in separated and free-shear regions, and WMLES in regions with sufficient resolution thereby reducing Reynolds number dependency (Shur et al., 2008). Further details of the formulations can be found in the Simcenter Star-CCM+ version 2020 User Guide (Siemens Digital Industries Software, 2020).

The governing equations are discretized using a hybrid second-order upwind/central difference scheme for spatial terms to balance numerical stability and accuracy, while a second-order implicit unsteady scheme is employed for temporal discretization. The system of algebraic equation resulting from the discretization was solved using a segregated algorithm where the conservation equations of mass and momentum are solved in a sequential manner.

3.2.2 Computational domain, boundary conditions and test conditions

The notchback model used is a 1:4 scaled downsize of the original Ahmed body (Ahmed et al., 1984). The model has a height, h = 72 mm, width, $W_b = 1.35h$ and length, L = 3.82h and a rounded fore-end with radius, R = 0.347h (figure.1). The notchback rear-end has a trunk of height $h_D = 0.687h$ and length, $L_D = 0.469h$ with a backlight and effective backlight angles, $\beta = 31.8^{\circ}$ and $\beta_e = 17.8^{\circ}$, respectively, resulting in a roof length, $L_S = 2.847h$. The ground clearance was set to G = 0.21h. As shown in (figure. 1), the left-handed Cartesian coordinate system adopted has the origin located at the midpoint of the lower edge of the back end of the model, with x, y and z in the streamwise, wall-normal and spanwise directions, respectively.

Figure 2 shows the computational domain and boundary conditions. The domain has a height of 6.0h and a width of 10.0h and length (D_t) of 30.8h. The leading edge of the Ahmed body is positioned at a streamwise distance of 8.0h from the domain inlet and the back end of the body is 19.0h from the domain outlet. A grid sensitivity test performed for the Re5E4 simulation (see table 3.1) using coarse (2.1×10^7) , medium (3.5×10^7) and fine (8.2×10^7) meshes showed good agreement between the medium and fine meshes. Based on the grid sensitivity test, the mesh used consists of 8.2×10^7 hexahedral elements with five levels of local refinement regions. The edges of the Ahmed body, identified as critical regions for inducing the asymmetric flow separation (He et al., 2021; Ouedraogo & Essel, 2024) were also refined. The mesh had 18 prism layers to accurately capture the near-wall flow characteristics, and the maximum $y^+ = 0.16$, where $y^+ = \frac{v_T y}{v}$, U_T is the friction velocity, y is the normal distance from the wall and v is the kinematic viscosity. Incompressible air flow at 25° C (where $\rho_{air} = 1.18 \, kgm^3$ and $\mu_{air} = 1.86 \, Pa \, s^{-1}$) was used as the working fluid. In terms of boundary conditions, the walls of the Ahmed body, the ground and side surfaces of the domain were set as no-slip condition while

the roof of the domain was set as free-slip conditions as demonstrated in figure. 3.2(a) and (b). Dirichlet boundary conditions of uniform freestream velocity, U_{∞} and constant pressure outlet were assigned to the inlet and outlet of the domain, respectively. The inlet velocity was set to $U_{\infty} = 2.18 \, m/s$ and $U_{\infty} = 10.88 \, m/s$, corresponding to Reynolds numbers of $Re_h = 1 \times 10^4$ (hereafter referred to as Re1E4) and $Re_h = 5 \times 10^4$ (Re5E4).

The non-dimensional time step $dt^* = \Delta t U_{\infty}/h$, where Δt is the time step, was set to 1.36×10^{-3} and 1.51×10^{-3} for the Re1E4 and Re5E4 case, respectively. This ensured a Courant-Friedrichs-Lewy (CFL) number less than 1 for both simulations. For each simulation, the solution was considered converged when the root-mean-square of the normalized residuals of the discretized equations were less than 10^{-6} . The transient data were sampled after two flow-through cycles, D_l/U_{∞} , for a duration of $tU_{\infty}/h = 50$, t is the physical time in seconds. This sampling duration captured more than 30 vortex shedding cycles ensuring a statistically converged solution (Sarkar & Sarkar, 2009). To characterize wake asymmetry, pressure coefficients (C_p) values were sampled in time from monitor points on both symmetric halves of the body at spacing distance of $d_z = 0.834h$ in the z-direction. As shown in figure. 3.2(c), the C_p values were obtained at the mid-length of the slant (s_l, s_r) , on deck (d_l, d_r) , and back of the trunk (b_l, b_r) , and the corresponding gradients determined as $\Delta C_p h/\Delta z$ for each section. Here, the subscripts "l" and "r" denotes the monitor points on the left and right side of the body, respectively. The wall-normal distance of the monitor points on the slant and back are $d_{y_2} = 0.844h$ and $d_{y_1} = 0.343h$, respectively. The monitored aerodynamic parameters (i.e. drag coefficient C_D , lift coefficient C_L , drift coefficient C_{Df} and C_p) were sampled at each time step for each test case.

Table 3.1	Summary	of grid	1 properties	for mesh	sensitivity	test of the Re	e5E4 simulation.
1 4010 3.1	Dullilliai	OI SIN	* brobernes	101 1110311	. DOLLDILL VIL V	tost of the it	CJL i billialanon.

Case	Cell count \times 10 ⁷	$\overline{C_D}$	$\overline{C_L}$	y_b^+	y_g^+
Coarse	2.1	0.326	0.169	0.808	0.533
Medium	3.5	0.372	0.152	0.860	0.533
Fine	8.2	0.370	0.151	0.164	0.156

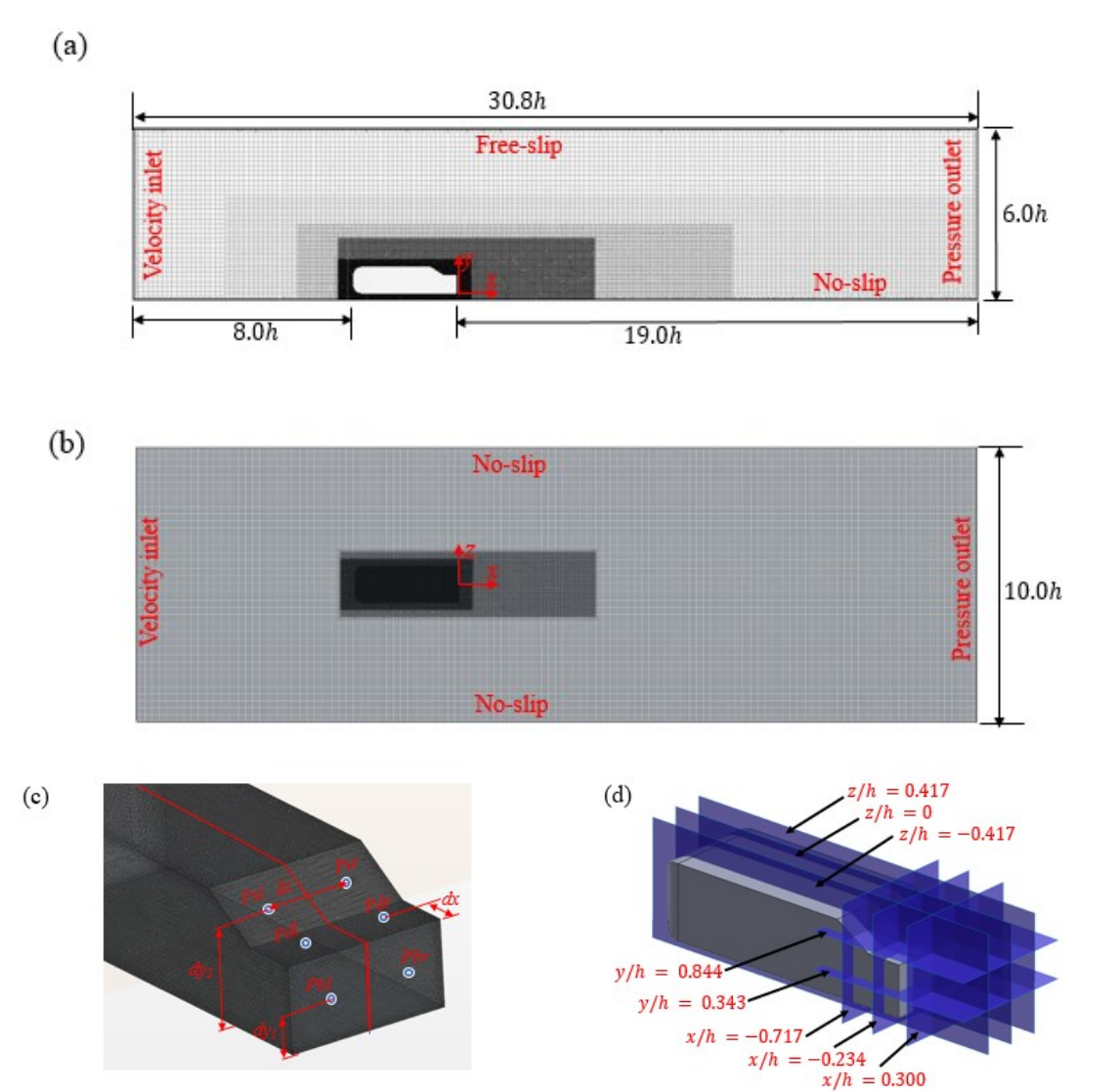


Figure 3.2: The computational domain and boundary conditions: (a) Side view of the mesh in the symmetry plane (z/h = 0), (b) top view of the mesh, (b) surface mesh on the rear end of the Ahmed body with dots representing pressure coefficient monitoring points and (d) two-dimensional planes used for investigations.

Moreover, instantaneous snapshots of the flow field at selected x - y and x - z planes (see figure. 3.2(d)) for both test cases were obtained at a strouhal number, sampling frequency of 926 Hz to further characterize the unsteady flow dynamics and the pumping motion of the recirculation regions.

The simulations were validated using the Re5E4 test case by comparing one-dimensional profiles of the streamwise mean velocity in the spanwise plane at y/h=0.343 and at streamwise locations, $l_{e1}-l_{e9}$ (0.03h away from the vertical back wall and with an interval of 0.1h) with corresponding profiles from LES and IDDES by He et al., (2021d), as shown in figure 3.3. The plots demonstrate that the present results agree with the LES and IDDES simulations by He et al. (2021d). Moreover, $\overline{C_D}=0.370$ and $\overline{C_L}=0.151$ for Re5E4 agree well with results of Sims-Williams et al. (2011) ($\overline{C_D}=0.370$) and He et al. (2021) ($\overline{C_D}=0.364$ and $\overline{C_L}=0.142$).

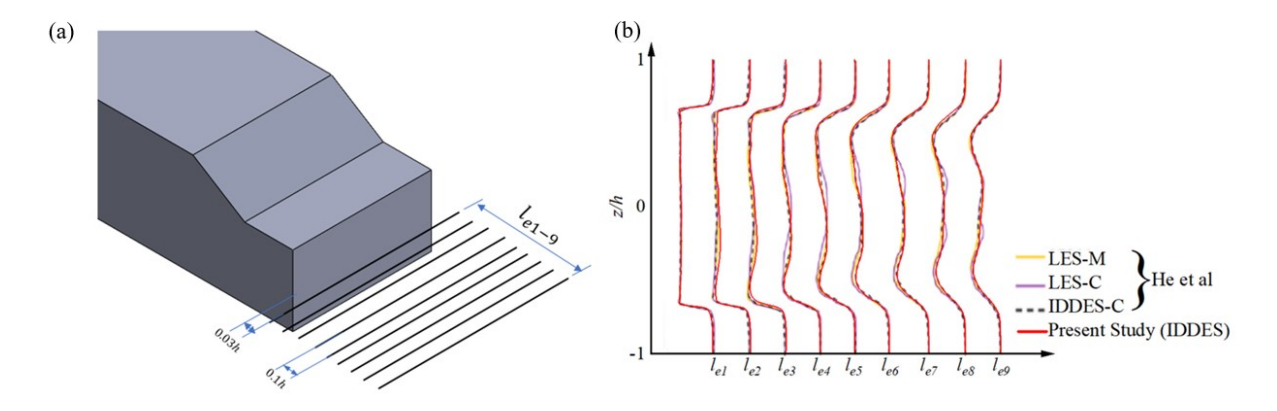


Figure 3.3: Profiles of mean streamwise velocity extracted in the spanwise plane at y/h = 0.343 and streamwise locations from l_{e1} (0.03h away from the vertical back) with an interval of 0.1h up to l_{e9} . The present results for Re5E4 are compared with the LES and IDDES profiles of He et al (2021), where – M and – C represent medium and coarse meshes, respective used in the previous study.

3.3 Results and discussion

The effects of Reynolds number on the wake characteristics of the notchback Ahmed body with an effective backlight angle of $\beta_e = 17.8^{\circ}$ were investigated using both 3D flow fields and 2D planes. As shown in figure 3.2(c), three streamwise-wall-normal (x - y) planes were extracted at the symmetry plane (z/h = 0) and at two offset planes $(z/h = \pm 0.417)$ to characterize wake asymmetry. For the streamwise-spanwise (x - z) planes, slices were obtained at the mid-height of the slant (y/h = 0.844) and behind the vertical back (y/h = 0.343). Moreover, cross-planes (y - z) at the mid-slant (x/h = -0.717), mid-deck (x/h = -0.234) and through the recirculation bubble behind the back (x/h = 0.300) were used to examine the streamwise vortical structures in the wake.

3.3.1 Mean flow characteristics

Figure 3.4 compares the contours of the streamwise mean velocity in the symmetry plane (z/h = 0) and offset planes (z/h = \pm 0.417) in the wake of Re1E4 and Re5E4. The mean streamlines are superimposed on the contours to reveal the flow pattern, while the green line, which represents the isopleth of U/U_{∞} = 0, is used to demarcate the boundaries of the reverse flow region (U/U_{∞} < 0) behind the body. The plus sign indicates the location of the maximum backflow (i.e., negative streamwise velocity) behind the back. For Re1E4, well-defined recirculation bubbles are formed over the slant and deck in the offset planes, but not in the symmetry plane, suggesting intermittent fully separated and attached flow in the symmetry plane. Behind the vertical back, the pairs of counter-rotating recirculation bubbles and their associated saddle points are similar in the offset planes; however, the anticlockwise bubble induced by the upwash is reduced compared to the clockwise bubble generated by the downwash, resulting in the saddle point being displaced closer to the wall in the symmetry plane. Moreover, the clockwise bubble shows a junction node

on the deck, highlighting a separated flow over the trailing edge of the deck. Unlike Re1E4, the recirculation bubble over the slant in the left offset plane (z/h = -0.417) for Re5E4 is significantly reduced compared to the right offset plane (z/h = +0.417). Furthermore, the bubble pair behind the back in the left offset plane is comparable to the structures in the offset planes of Re1E4. However, the clockwise bubble in the right offset plane of Re5E4 is substantially enhanced, leading to a downward displacement of the associated saddle point. In the symmetry plane, Re5E4 exhibits a well-defined recirculation bubble over the slant and a clear separation point at the trailing edge of the deck, in contrast to Re1E4. These results indicate that Re1E4 generates a symmetric mean wake, whereas Re5E4 induces an asymmetric wake, consistent with previous studies (Sims-Williams et al., 2011; He et al., 2021; Ouedraogo & Essel, 2024).

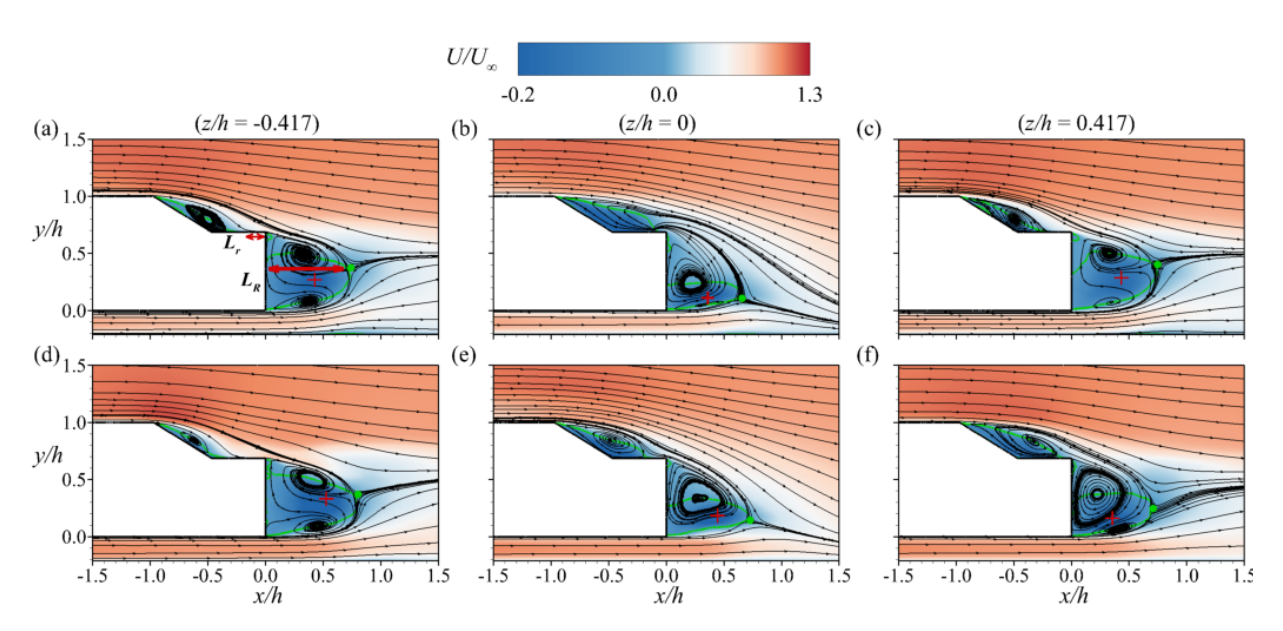


Figure 3.4: Contours of normalized streamwise mean velocity, U/U_{∞} in the symmetry plane (z/h=0) and offset planes $(z/h=\pm 0.417)$, superimposed with mean streamlines for (a-c) Re1E4 and (d-f) Re5E4. The green line represents the isopleth of $U/U_{\infty}=0$ which bounds the reverse flow region $(U/U_{\infty}<0)$. The plus (+) sign shows the locus of the maximum backflow velocity and the green dot (•) represents the saddle point.

Table 3.2 Summary of the mean reverse flow parameters for Re1E4 and Re5E4.

Case	Plane (z/h)	A_r/h^2	L_r/h	U_r^b/U_∞	A_R/h^2	L_R/h	U_R^b/U_∞
Re1E4	-0.417	0.06	0.23	-0.13	0.15	0.74	-0.20
Re1E4	0	0.20	0.07	-0.26	0.10	0.65	-0.24
Re1E4	0.417	0.07	0.19	-0.13	0.16	0.74	-0.16
Re5E4	-0.417	0.05	0.32	-0.12	0.17	0.80	-0.27
Re5E4	0	0.10	0.12	-0.25	0.12	0.73	-0.26
Re5E4	0.417	0.12	0.06	-0.18	0.13	0.71	-0.21

The characteristics of the mean recirculation bubbles over the slant and behind the back are summarized in table 3.2. The normalized mean reverse flow areas over the slant and behind the back are denoted as A_r/h^2 and A_R/h^2 , respectively, and the corresponding normalized maximum backflow velocities are U_r^b/U_∞ and U_R^b/U_∞ , respectively. The reattachment length, L_r/h , is defined as the normalized streamwise distance from the reattachment point on the deck to the trailing edge of the deck. Similarly, the recirculation length, L_R/h , is defined as the normalized streamwise distance from the back to the saddle point S_p . Each mean reverse-flow area is determined as:

$$A = \int_{N} \int_{M} \mathcal{H}(u(x, y, t) < 0) \ dx \, dy; \tag{3.4}$$

where H is the detector function, u(x, y, t) is the instantaneous streamwise velocity, dx and dy are the vector spacings in the x and y directions, respectively, M is the integration area over the slant-deck region or behind the vertical back, and N is the total number of snapshots used, i.e., $N \approx 1900$ and 380 for Re1E4 and Re5E4, respectively. It is noteworthy that, despite the difference in sample size between the two cases, the total sampling time captured (i.e., $tU_{\infty}/h = 50$) at a frequency of 926 Hz is similar for both. The integration area M was fixed at $x/h \in [-1.0, 0.0]$ and

 $y/h \in [0.7, 1.0]$ for the slant-deck region, and $x/d \in [0.0, 1.1]$ and $y/d \in [0.0, 0.7]$ behind the back.

For the slant-deck region, $A_r/h^2 \approx 0.06$, $L_r/h \approx 0.21$ and $U_r^b/U_\infty = -0.13$ in the offset planes of Re1E4, however, the area and backflow increase to $A_r/h^2 = 0.20$ and $U_r^b/U_\infty = -0.26$, respectively, while the reattachment length reduces to $L_r/h = 0.07$ in the symmetry plane. On the other hand, for Re5E4, the left offset plane shows $A_r/h^2 = 0.05$ and $U_r^b/U_\infty = -0.12$, which increase to $A_r/h^2 = 0.12$ and $U_r^b/U_\infty = -0.18$ in the right offset plane. As a result, the reattachment length decreases from $L_r/h = 0.32$ on the left side to $L_r/h = 0.06$ on the right side of the deck. In the symmetry plane of Re5E4, $A_r/h^2 = 0.10$, $L_r/h = 0.12$ and $U_r^b/U_\infty = -0.25$. Behind the vertical back of Re1E4, $A_R/h^2 \approx 0.15$, $L_R/h \approx 0.74$ and $U_R^b/U_\infty = -0.18 \pm 0.02$ in the offset planes but reduces in the symmetry plane, $A_R/h^2 \approx 0.10$, $L_R/h \approx 0.65$ and $U_R^b/U_\infty = -0.24$ due to downwash effects. For Re5E4, the degree of asymmetry in the reverse flow parameters is reduced in the wake. For example, the difference in reverse flow area between the offset planes is approximately 30%, compared to 58% on the slant.

Figure 3.5 presents contours of the normalized wall-normal mean velocity, V/U_{∞} . In the offset planes of Re1E4, the downwash (i.e., V < 0) is intense over the slant and deck but reduced behind the back. However, the upwash (V > 0) behind the back is significantly enhanced, resulting in the high y-location of the saddle point. In the symmetry plane, however, the downwash is more pronounced and extends further into the wake region, shifting the saddle point closer to the wall. For Re5E4, the downwash over the slant is dominant in the left offset plane, leading to a reduced recirculation bubble and an earlier reattachment point compared to the right offset plane. The

downwash and upwash patterns in the symmetry plane of Re5E4 are qualitatively similar to those of Re1E4, but with a more intense downwash.

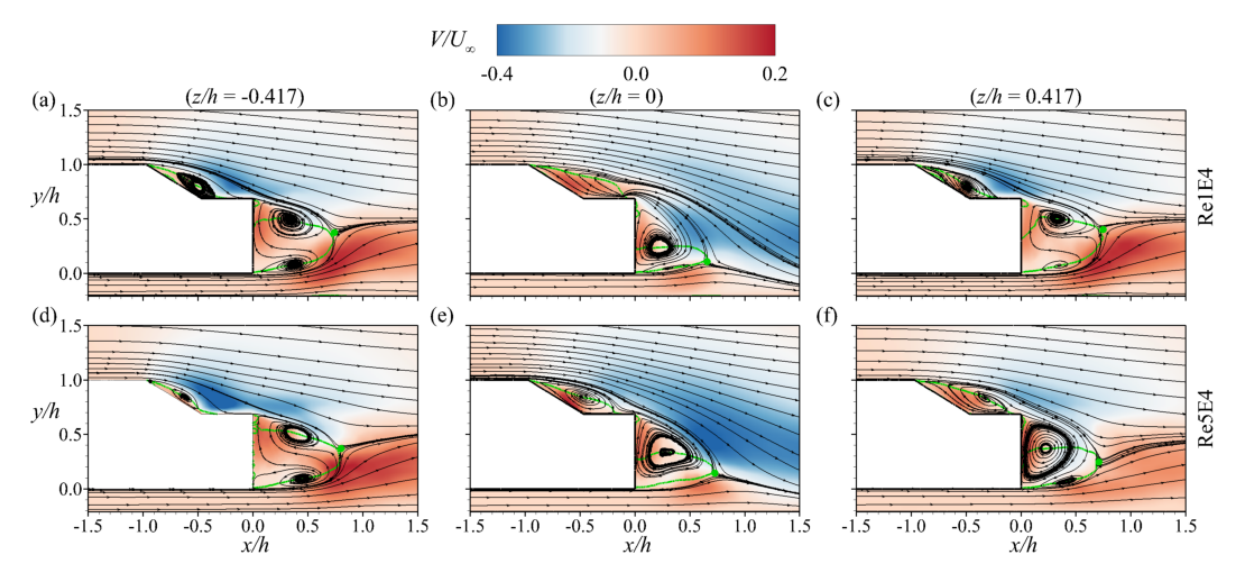


Figure 3.5: Contours of normalized wall normal mean velocity V/U_{∞} , superimposed with mean streamlines. The green line represents the isopleth of $U/U_{\infty} = 0$ which bounds the reverse flow region $(U/U_{\infty} < 0)$ and the green dot (\bullet) represents the saddle point.

Contours of the normalized spanwise mean velocity (W/U_{∞}) in the horizontal planes at the mid-height of the slant (y/h = 0.844) and the mid-height of the vertical back (y/h = 0.343) are shown in figure 3.6. For Re1E4, the reverse flow regions and W/U_{∞} at both planes are nearly symmetric, however, the mean streamlines exhibit strong interactions across the sides of the body. Behind the back, a large vortex is present on the left side (z/h < 0) but absent on the right (z/h > 0), suggesting that the toroidal structure in the wake of Re1E4 is asymmetric. In contrast, Re5E4 exhibits a reverse flow region skewed toward the right side (z/h > 0), attributed to enhanced entrainment on the left. Moreover, several small-scale vortices are evident behind the back, and the reverse flow region displays a higher degree of asymmetry compared to Re1E4.

Figure 3.7 shows the mean streamlines and contours of the mean pressure coefficient, $\overline{C_p} = 2(p - p_{\infty})/\rho U_{\infty}^2$, in three cross-planes (x/h = -0.717, -0.234 and 0.300) behind the body for

Re1E4 and Re5E4, where p is the mean static pressure and p_{∞} is the freestream atmospheric pressure. For Re1E4, the mean streamlines and pressure coefficient exhibit a symmetric distribution about the symmetry plane (z/h=0). The cross-planes at x/h=-0.717 and -0.234 reveal the characteristic lower vortex structures of the Ahmed body. On the deck, traces of the C-pillar vortices are visible near the upper corners, while a junction vortex forms near the centerline, induced by the separated flow reattaching on the deck. Behind the back (x/d=0.3), the streamlines show the footprint of a toroidal structure. In contrast, for Re5E4, the contours of $\overline{C_p}$ exhibit strong negative pressure on the left side of the slant and the right side of the deck, attributed to the asymmetric reverse flow region and reattachment on the deck. As a result, the C-pillar vortices also show pronounced asymmetry. Furthermore, the number of lower vortical structures increases for Re5E4. Behind the back, the streamlines demonstrate stronger asymmetric entrainment and downwash compared to Re1E4.

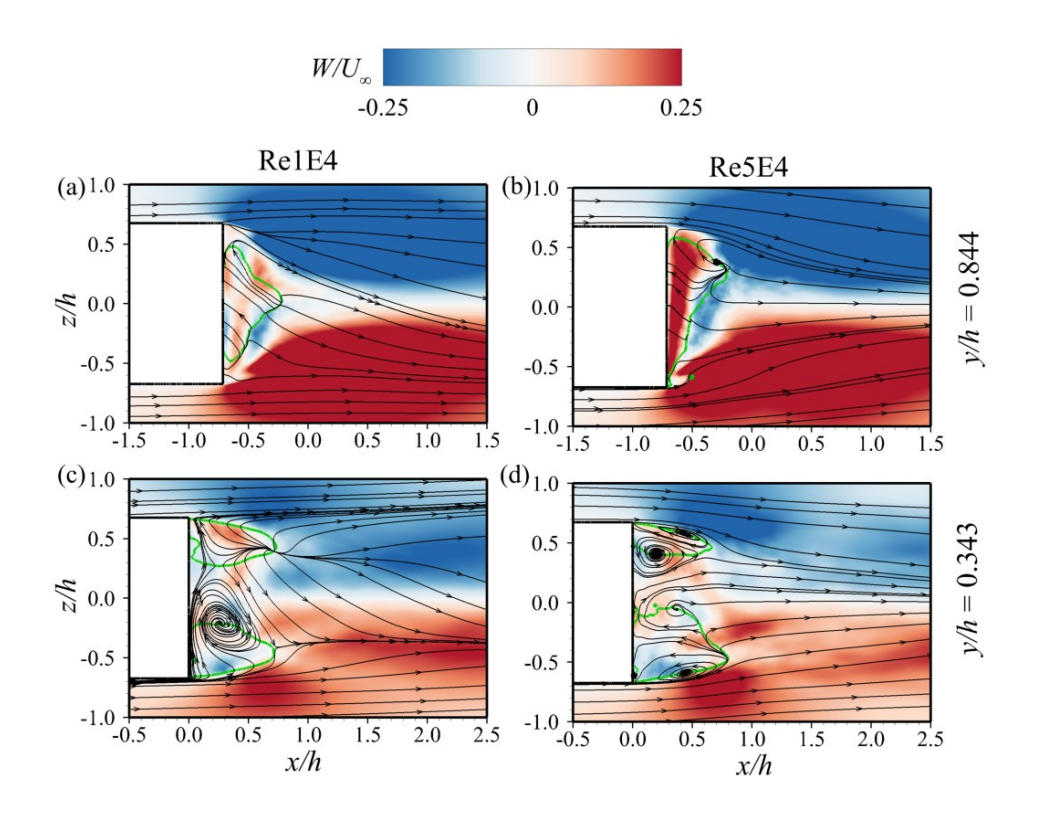


Figure 3.6: Contours of normalized spanwise mean velocity W/U_{∞} in the horizontal planes (a, b) at y/h = 0.844 and (c, d) y/h = 0.343 for Re1E4 and Re5E4.

To examine the 3D wake structure, iso-surfaces of the mean Q-criterion (Hunt et al., 1988) and the reverse flow volume $(U/U_{\infty} < 0)$ are presented in figure 3.8. A threshold of $Q(h/U_{\infty})^2 = 3.7$ was applied to capture the dominant vortical structures, including the C-pillar vortices (denoted as V_l and V_r) and the spanwise shear layers emanating from the trailing edge of the roof, labeled as V_c . The Q-criterion iso-surfaces are colored by the spanwise mean vorticity. The plots reveal asymmetric 3D vortical structures and reverse flow volumes in Re5E4 compared to Re1E4, consistent with the asymmetries observed in the 2D planes.

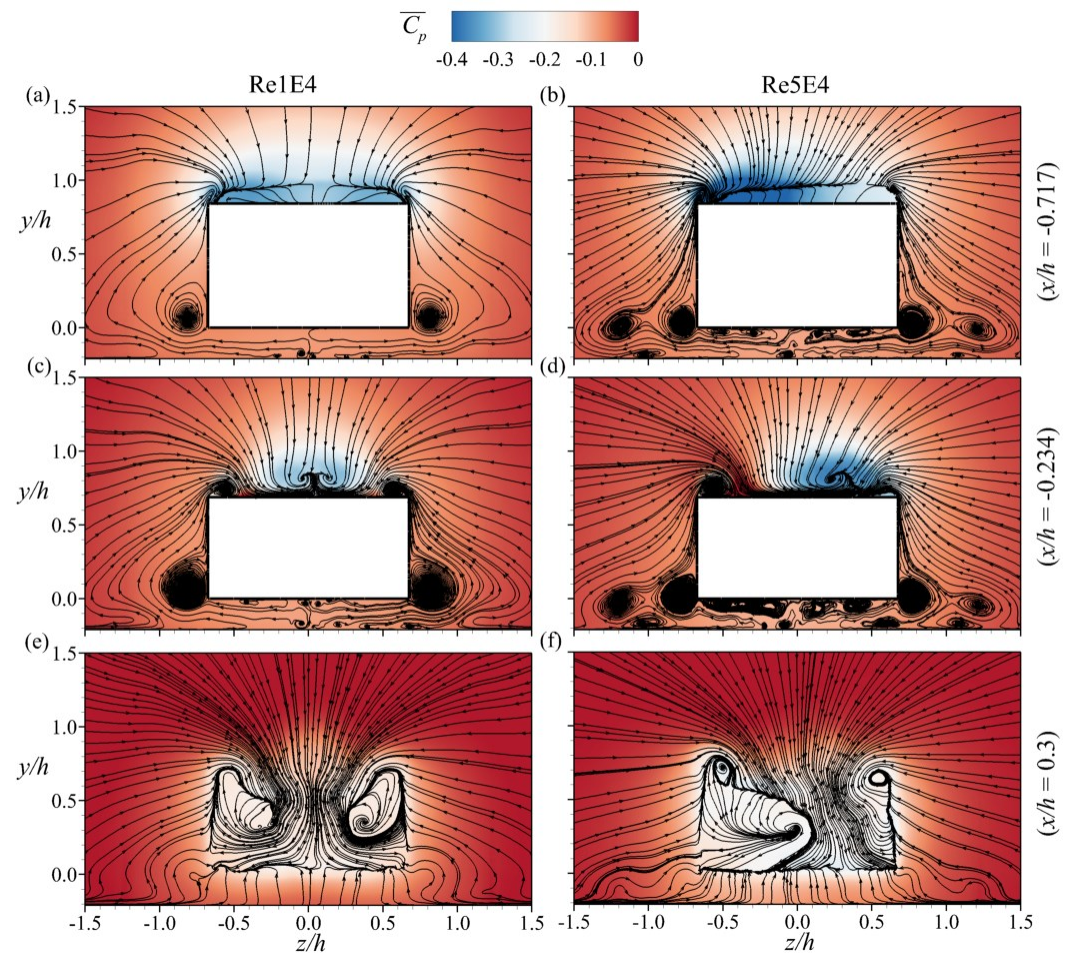


Figure 3.7: Contours of the mean pressure coefficient in the cross planes at (a, b) x/h = -0.717, (c, d) x/h = -0.234 and (e, f) x/h = 0.3 for Re1E4 and Re5E4.

3.3.2 Turbulence statistics

Figure 3.9 compares the contours of Reynolds normal stresses ($\overline{u'u'}$, $\overline{v'v'}$, $\overline{w'w'}$) in the symmetry plane (z/h=0) and offset planes ($z/h=\pm 0.417$) for Re1E4 and Re5E4. The Reynolds stresses are enhanced in the separated shear layer over the slant, as well as in the downwash and upwash shear layers behind the back, due to strong mean shear in these regions. In the symmetry plane of Re1E4, the normal stresses are more pronounced in the separated shear layer over the slant and in the upwash region compared to the downwash. In contrast, in the offset planes, the streamwise and wall-normal Reynolds stresses are enhanced in the downwash behind

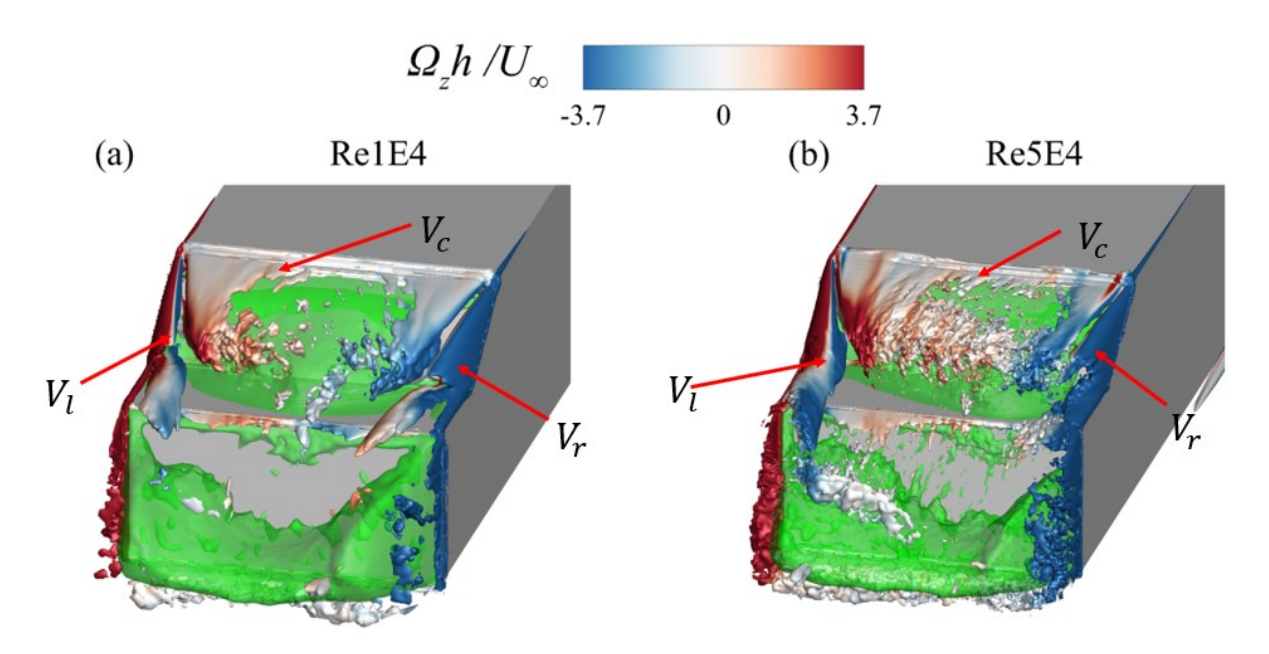


Figure 3.8: Three-dimensional mean flow topology in the near wake of (a) Re1E4 case, and (b) Re5E4 case, visualized using the iso-surfaces of the mean Q-criterion $(Q(h/U_{\infty})^2 = 3.7)$ and reverse flow volume $(U/U_{\infty} = 0, i.e., green region)$.

the back than in the slant shear layer or the upwash. The spanwise Reynolds normal stress, on the other hand, exhibits larger intensity in the upwash region compared to the other shear layers. Near the ground, the streamwise Reynolds stress increases due to the interaction between the upwash and the wall. The Reynolds stresses for Re5E4 are generally more intense than those for Re1E4. Unlike Re1E4, the stresses in Re5E4 exhibit significant asymmetry, with higher magnitudes on the right side. This asymmetry is most pronounced in $\overline{u'u'}$ compared to $\overline{v'v'}$ and $\overline{w'w'}$. For instance, the maximum streamwise Reynolds normal stress on the right side increases by approximately 52% in the slant shear layer and 32% in the upwash region compared to the left side. In contrast, the wall-normal component increases by 30% in the slant shear layer but decreases by 17% in the upwash. The spanwise component exhibits increases of 44% and 5% in the respective shear layers across the offset planes. It is also interesting to note that, unlike the right side, the earlier reattachment followed by separation at the trailing edge of the deck on the left side induces a stronger downwash shear layer, which is associated with more intense Reynolds stresses. On the right side, reattachment occurs much closer to the trailing edge, resulting in a less developed downwash shear layer as the slant shear layer overshoots further into the wake.

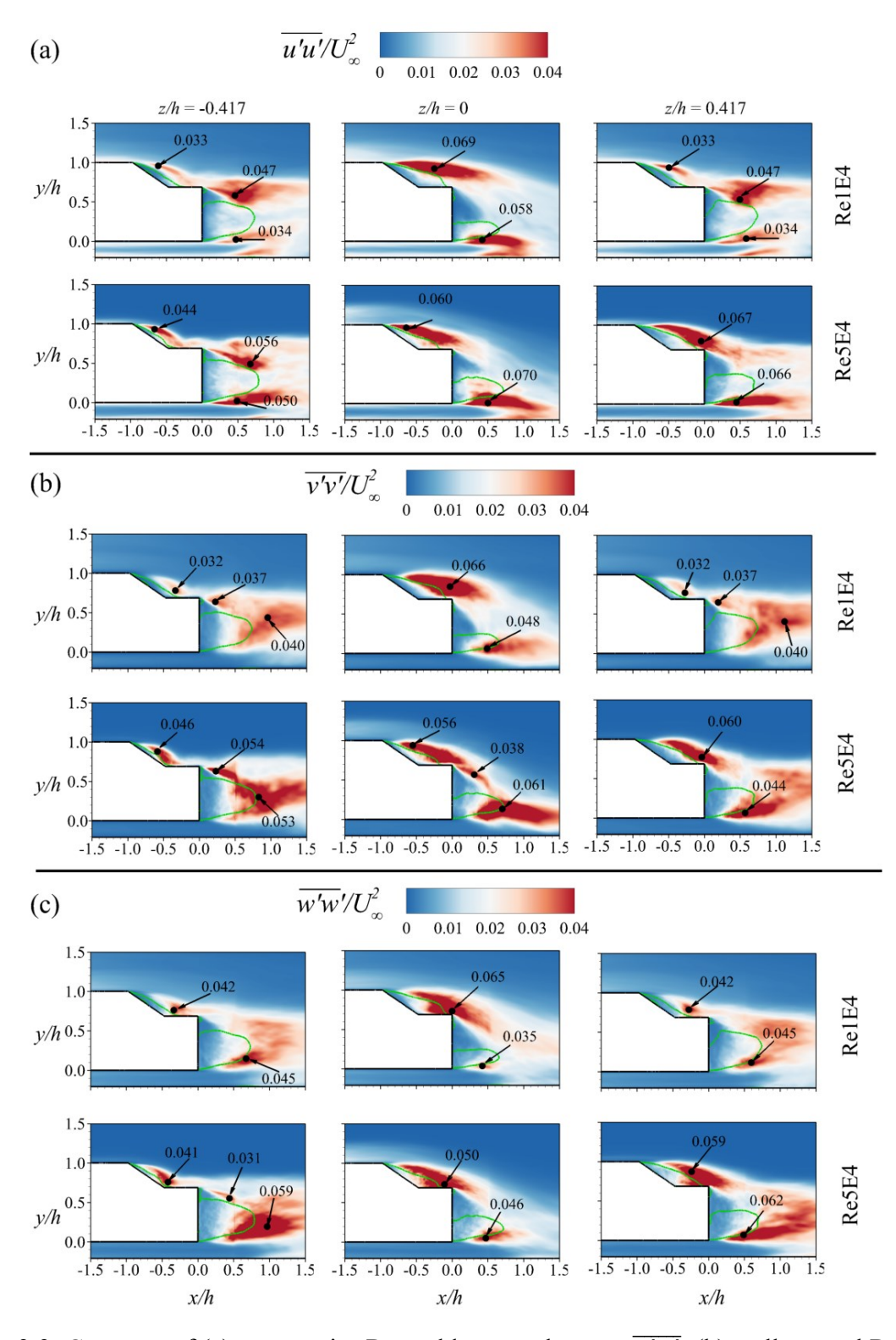


Figure 3.9: Contours of (a) streamwise Reynolds normal stress, $\overline{u'u'}$, (b) wall normal Reynolds normal stress $\overline{v'v'}$ and (c) spanwise Reynolds normal stress $\overline{w'w'}$ in the vertical planes for Re1E4 and Re5E4.

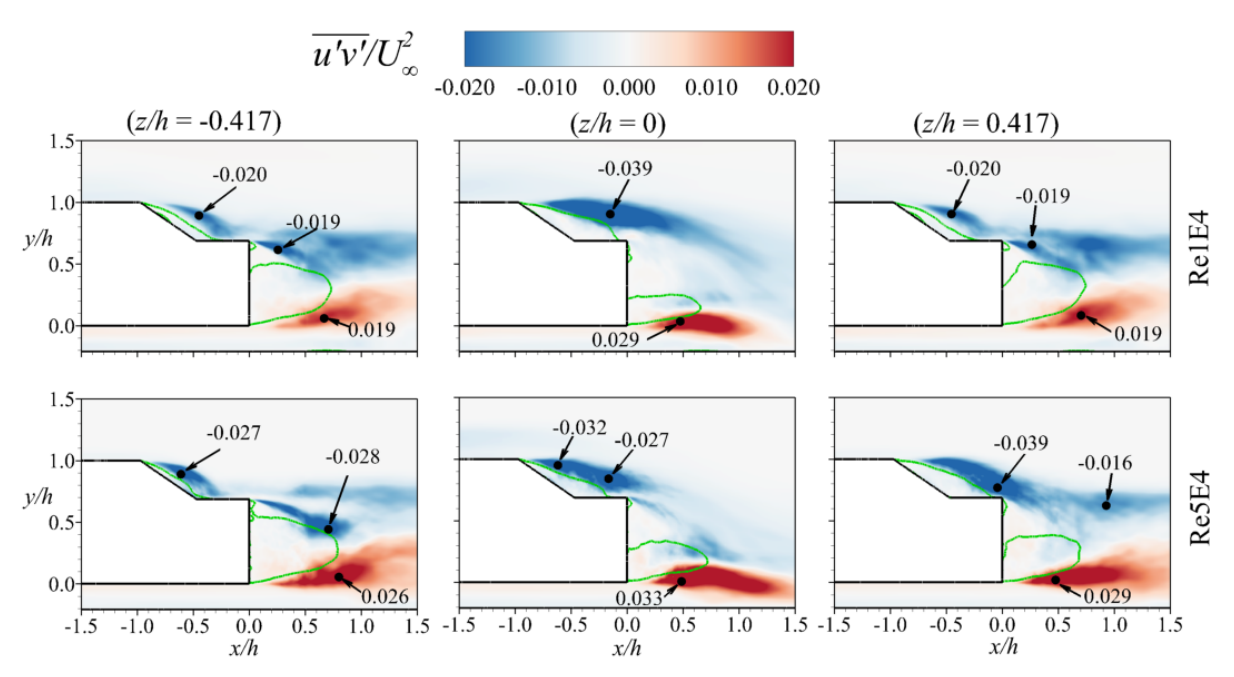


Figure 3.10: Contours of normalized Reynolds shear stress, $\overline{u'v'}$ for Re1E4 and Re5E4 in the vertical planes z/h = 0 and $z/h = \pm 0.417$.

Contours of the Reynolds shear stress $(\overline{u'v'})$ are presented in figure 3.10. The Reynolds shear stress exhibits negative values within the slant and downwash shear layers, and positive values in the upwash shear layer, consistent with the orientation of the mean shear $(\partial U/\partial y)$. The influence of Reynolds number on the shear stress distribution is qualitatively similar to its effect on the Reynolds normal stresses, with higher magnitudes and increased asymmetry observed at Re5E4 compared to Re1E4.

The effects of Reynolds number on large-scale anisotropy in the wake of the notchback are investigated using the anisotropy tensor (b_{ij}) defined as

$$b_{ij} = \frac{\overline{u_i u_j}}{\overline{u_i u_i}} - \frac{1}{3} \delta_{ij} \tag{3.5}$$

where δ_{ij} is the Kronecker delta and b_{ij} is traceless (i.e., $b_{ii}=0$). To quantify the deviation from isotropy, the relative contributions of the Reynolds normal stresses to the turbulent kinetic energy $(k=0.5\overline{u_iu_i})$ are examined through the diagonal components, b_{11} , b_{22} and b_{33} . These

components can have values that range from -2/3 to 4/3, with a value of zero indicating isotropy (Kang et al., 2021; Pope, 2000). Figure 3.11 presents contours of b_{11} , b_{22} and b_{33} for Re1E4 and Re5e4. The flow over the roof into the wake, within the reverse flow region behind the back, and in the underbody flow near the wall exhibits strong anisotropy. In these regions, b_{11} shows enhanced positive values, while b_{22} and b_{33} are negative, indicating that the streamwise Reynolds stress is the dominant contributor to the turbulent kinetic energy. Within the reverse flow region over the slant, b_{33} (i.e., associated with the spanwise Reynolds normal stress) is dominant. In contrast, in the downwash and upwash shear layers, as well as downstream of the reverse flow region behind the back, b_{22} (associated with wall-normal Reynolds normal stress) is more pronounced, reflecting the influence of vortex shedding in the wake. The wake asymmetry induced at Re5E4 is also evident in the large-scale anisotropy. Unlike Re1E4, the offset planes of Re5E4 exhibit significant differences, particularly within the reverse flow region behind the back and in the associated shear layers. Moreover, the level of anisotropy tends to increase with Reynolds number.

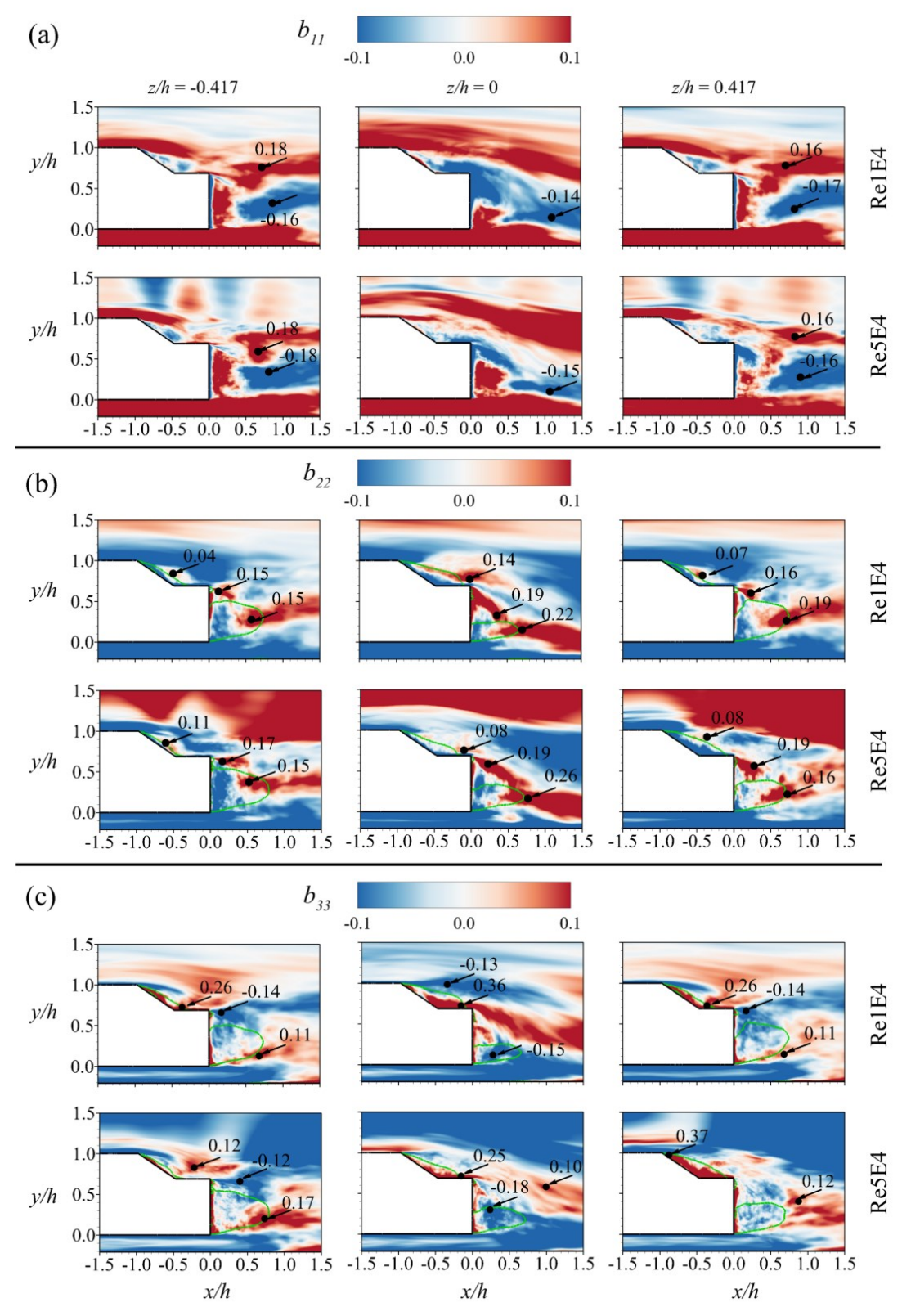


Figure 3.11: Contours of turbulence anisotropy, (a) b_{11} , (b) b_{22} and (c) b_{33} in the vertical planes z/h = 0 and $z/h = \pm 0.417$ for Re1E4 and Re5E4.

To investigate the dominant sources of turbulent kinetic energy and anisotropy, the production terms of the transport equations of the Reynolds normal stresses and turbulent kinetic energy are evaluated as:

$$P_{ii} = -2\left(\overline{u_i u_k} \frac{\partial U_i}{\partial x_k}\right) \tag{3.6}$$

$$P_k = P_{ii}/2 \tag{3.7}$$

where P_{ii} is the trace of the Reynolds stress production tensor, and P_k denotes the production of turbulent kinetic energy. The individual components of P_{ii} include P_{11} (denoted as P_{uu}), which represents the production of the streamwise Reynolds normal stress; $P_{22} = P_{vv}$, the production of wall-normal Reynolds normal stress; and $P_{33} = P_{ww}$, the production of spanwise Reynolds normal stress.

Figure 3.12 shows that the production of turbulent kinetic energy (P_k) is most intense within the separated shear layer over the slant and in the downwash and upwash shear layers behind the back. These intense production regions are due to the combined effects of large Reynolds shear stress (Figure 3.10) and strong mean shear ($\partial U/\partial y$) in the shear layers. For Re1E4, the production is higher in the symmetry plane compared to the offset planes. Additionally, the production of turbulent kinetic energy increases with Reynolds number. However, unlike Re1E4, Re5E4 exhibits greater production over the slant on the right side than on the left, while the production in the downwash shear layer is more intense on the left side than on the right. This asymmetry is consistent with the previously observed differences in the mean flow structure and Reynolds stresses.

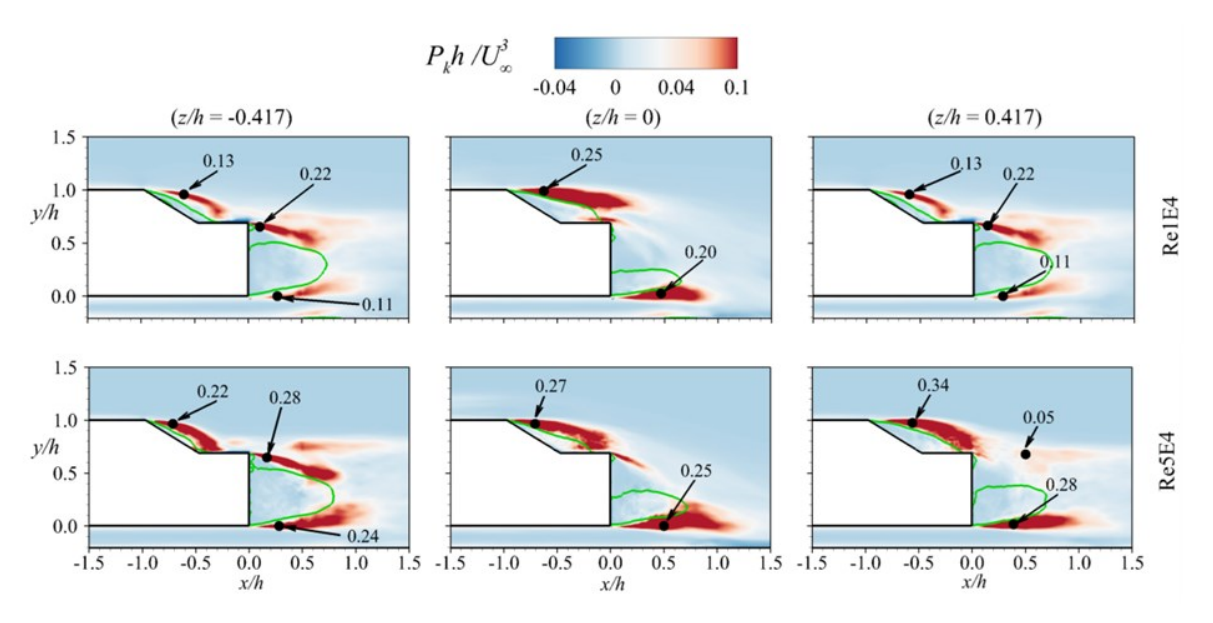


Figure 3.12: Contours of normalized production of turbulence kinetic energy (P_k) in the vertical planes, z/h = 0 and $z/h = \pm 0.417$ for Re1E4 and Re5E4.

Contours of the individual production terms, P_{uu} , P_{vv} and P_{ww} , are presented in figure 3.13. It is immediately evident that P_{uu} is the dominant contributor to turbulent kinetic energy production (figure 3.12) in the shear layers over the slant and behind the back. However, near the reattachment point on the deck and in the downstream region of the reverse flow behind the back, P_{uu} is negative, indicating local energy sinks. These regions of negative P_{uu} are compensated by significantly larger positive values of P_{vv} and P_{ww} , resulting in a net positive production of turbulent kinetic energy (figure 3.12) in these areas. Similarly, areas of negative P_{vv} or P_{ww} are offset by contributions from the other components, demonstrating the redistribution of energy among the Reynolds stresses. Furthermore, the presence of sustained Reynolds normal stress (figure 3.9) in regions of negative production emphasizes the role of the pressure-strain term in the transport equation of the Reynolds normal stresses, which transfer energy across components to offset local deficits. This interplay highlights the strong anisotropy in the wake of the notchback geometry. Consistent with the effects of Reynolds number on the Reynolds stresses, the production terms for Re5E4 exhibit notable asymmetry and differ from those observed for Re1E4. For example, for

Re5E4, P_{uu} is significantly enhanced in the slant shear layer on the right side compared to the left, and in the downwash shear layer on the left side compared to the right, in agreement with the contours of the streamwise Reynolds normal stress (Figure 3.9(a)).

Figure 3.14 shows the contours of the Reynolds stresses $(\overline{u'u'}, \overline{v'v'}, \overline{u'u'})$ and $\overline{u'w'}$ in the spanwise planes (y/h = 0.343 and 0.844). The Reynolds normal stresses are significantly enhanced within the spanwise shear layers over the slant and behind the back. For Re5E4, the regions of high stresses over the slant are skewed toward the right side (z/h > 0), in contrast to the more symmetric distribution of Re1E4. However, the asymmetry in the stress distribution behind the back for Re5E4 is less pronounced than that observed over the slant. For the Reynolds shear stresses, the alternating signs in the contours over the slant for Re1E4 indicate the presence of the spanwise shear layers, flanked by side shear layers associated with the C-pillar vortices. Downstream of the back, these C-pillar vortices become more pronounced, as evidenced by the broader regions of oppositely signed shear stress extending along the sides of the wake. The contours over the slant for Re5E4 suggest that asymmetry significantly distorts the formation of the right-side C-pillar vortex, consistent with earlier observations from the cross-plane and Qcriterion plots (Figures 3.7 and 3.8). This asymmetry also manifests behind the back, where the distribution of Reynolds shear stress for Re5E4 appears disrupted compared to the well-ordered pairs observed in Re1E4.

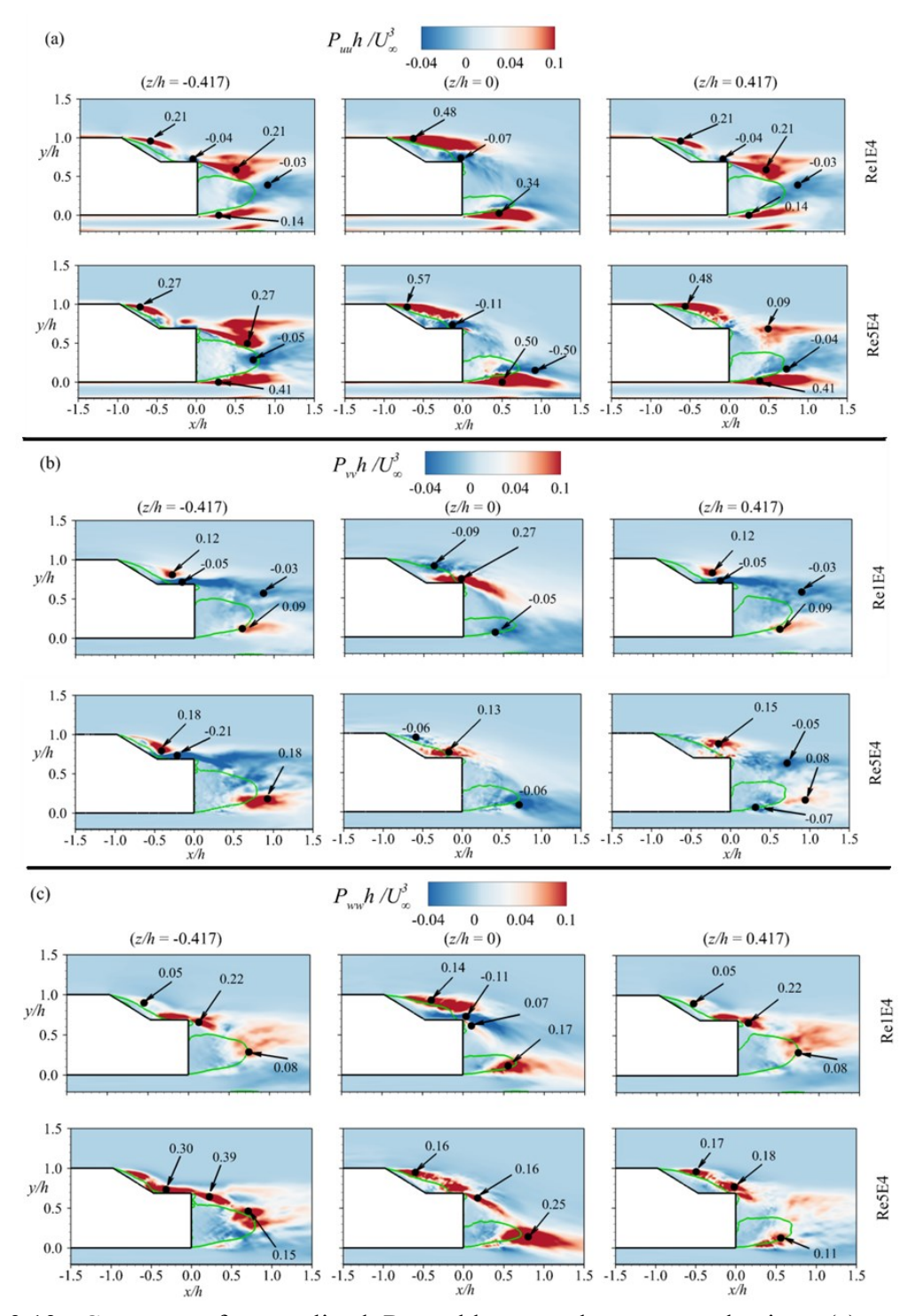


Figure 3.13: Contours of normalized Reynolds normal stress production: (a) streamwise production P_{uu} , (b) wall normal production P_{vv} and (c) spanwise production P_{ww} .

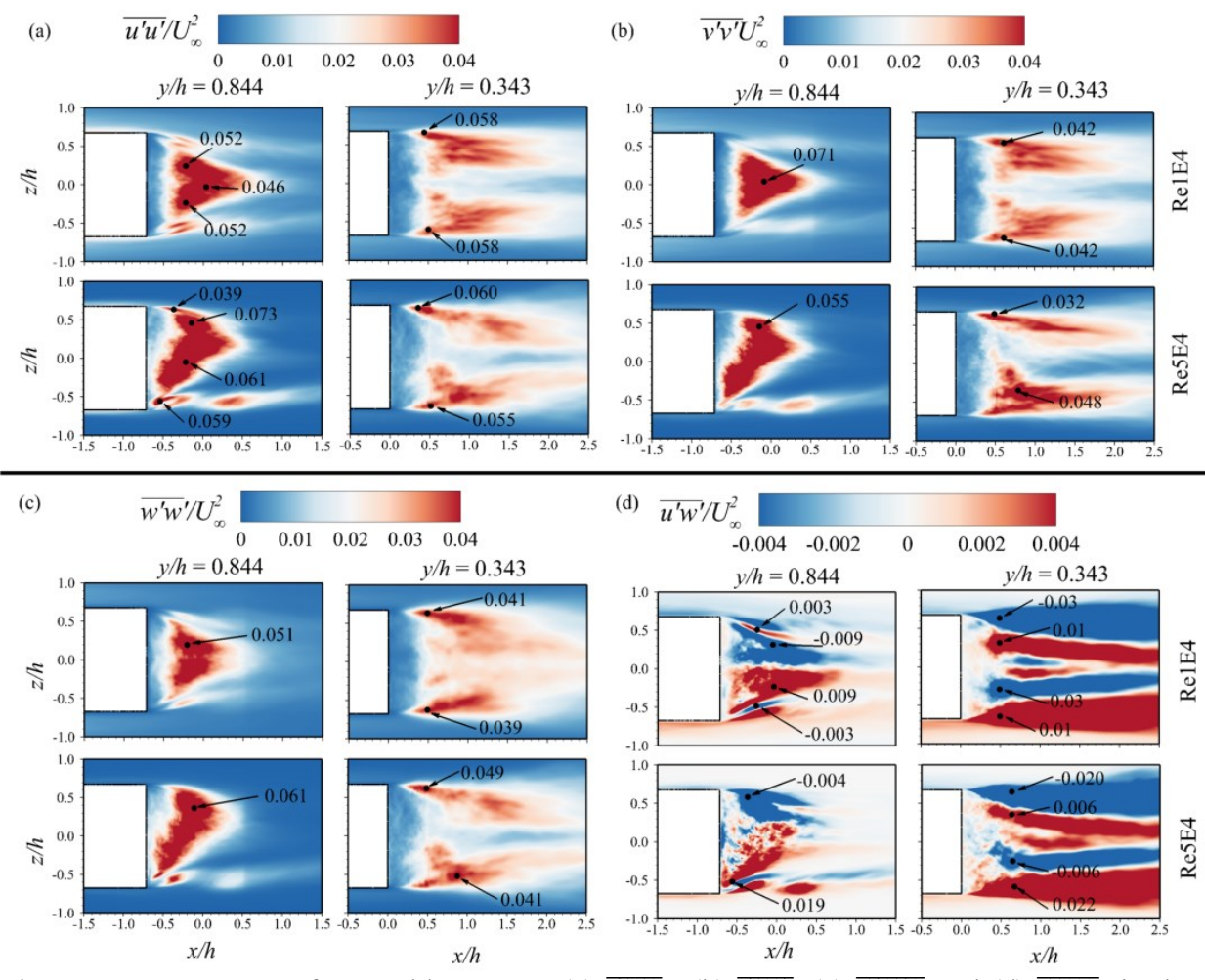


Figure 3.14: Contours of Reynolds stresses (a) $\overline{u'u'}$, (b) $\overline{v'v'}$, (c) $\overline{w'w'}$ and (d) $\overline{u'w'}$ in the spanwise planes at y/h = 0.844 and y/h = 0.343 for Re1E4 and Re5E4.

3.3.3 Instantaneous vortical structures and global dynamics

The unsteady 3D wake structures of the notchback geometry result from complex interactions between multiple shear layers undergoing energetic oscillations induced by flow instabilities and vortex shedding. These dynamics significantly influence the global behavior of the wake and can lead to persistent asymmetries and mode switching phenomena, such as bimodality and trimodality (Grandemange et al., 2013; He, et al., 2021; He, et al., 2021b). The wake asymmetry originates from the first steady instability in the laminar regime (Grandemange et al., 2012), and

the onset of mode switching is stochastic, often occurring after a large characteristic timescale. For example, in the case of a squareback Ahmed body, the switching timescale is approximately $1000h/U_{\infty}$ (Grandemange et al., 2013b, 2013a; Volpe et al., 2015). In contrast, He et al. (2021) observed the first bimodal switch for a notchback with $\beta_e = 17.8^{\circ}$ after a timescale of about $96h/U_{\infty}$, with the asymmetric state persisting for over $830h/U_{\infty}$ timescale.

The influence of Reynolds number on the wake asymmetry of the notchback is examined using instantaneous vortical structures visualized by iso-surfaces of the Q-criterion. The iso-surfaces are colored by the normalized instantaneous spanwise velocity, w/U_{∞} , to highlight the directional bias of the vortex-induced motions, which is important for assessing wake asymmetry. Representative visualizations for each test case are shown in figure 3.15, where a high Q-criterion threshold of $Q(h/U_{\infty})^2 = 80$ is used to isolate the more energetic and coherent structures. Here, negatively signed vortices are associated with spanwise motion toward the left side of the body

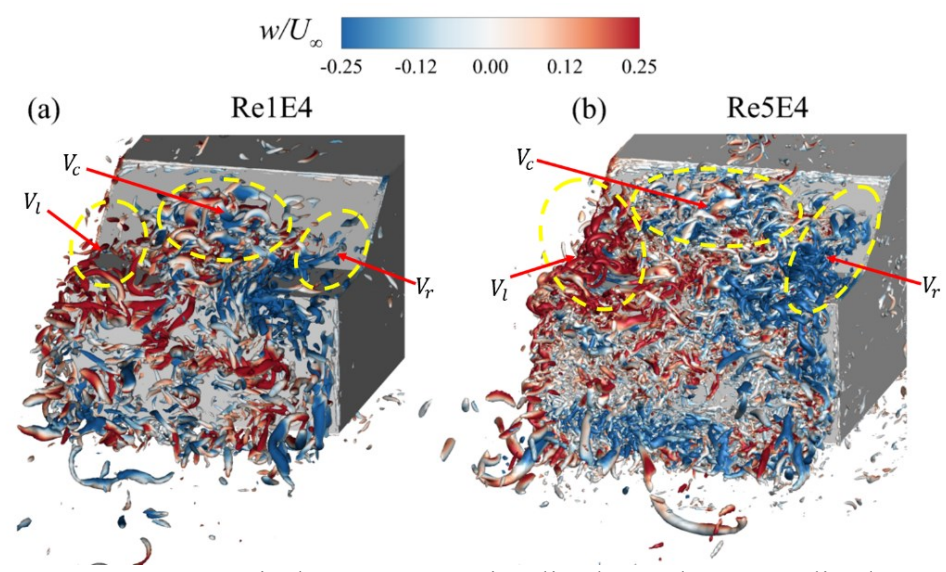


Figure 3.15: Instantaneous vortical structures visualized at the normalized Q-criterion value $Q(h/U_{\infty})^2 = 80$ for Re1E4 and Re5E4 cases colored by the normalized instantaneous spanwise velocity (w).

(i.e., left-bound), while positively signed vortices correspond to motion toward the right side (i.e., right-bound). For both Reynolds numbers, left-bound vortices are dominant on the right side, while right-bound vortices are more prominent on the left, consistent with the direction of spanwise entrainment from the sides. Similar to the labeling in figure 3.8, the vortical structures primarily associated with the spanwise shear layer from the roof are denoted as V_c , while the C-pillar vortices are labeled V_l and V_r for the left and right sides, respectively. For Re1E4, the V_c vortices are clustered near the mid-span of the slant, with near-symmetric distribution of V_l and V_r on either side. In contrast, for Re5E4, the V_c vortices are predominantly left-bound and displaced toward the left side of the slant. On the deck, right-bound vortices are more dominant, with several extending across the symmetry plane toward the right-side of the body, highlighting a pronounced asymmetry. Behind the back, the vortical structures of Re5E4 appear less organized with persistent left-bound vortices in the upwash shear layer compared to Re1E4.

To further investigate the unsteady characteristics of the wake, the temporal histories and probability density functions (PDFs) of the spanwise gradients of the instantaneous pressure coefficient, $\Delta C_p h/\Delta z$, on the slant, deck, and back, as well as the drag (C_D) , lift (C_L) and drift (C_{Df}) coefficients, are presented in figure 3.16. For Re1E4, the temporal histories of $\Delta C_p h/\Delta z$ on the slant and back are weak and identically zero, demonstrating symmetry. On the deck, the gradient tends to remain on either side of zero for short durations but switches direction frequently, resulting in a broader, Gaussian-like PDF centered near zero. In contrast, for Re5E4, the pressure gradient on the slant is predominantly positive, while on the deck it is mostly negative, with values remaining near zero for the gradient on the back. Accordingly, the PDFs for the slant and deck are centered at 0.27 and -0.74, respectively.

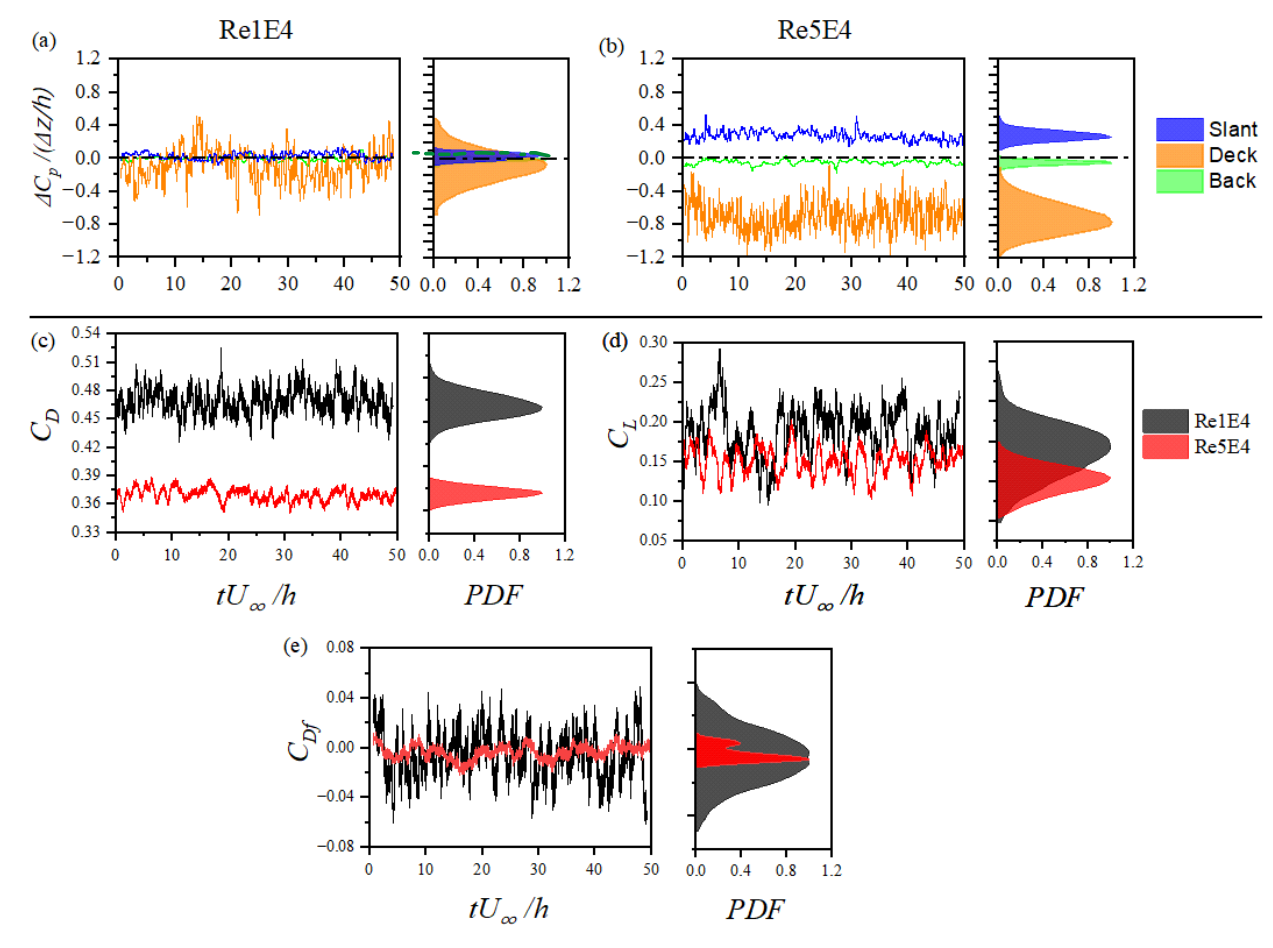


Figure 3.16: Temporal history (tU_{∞}/h) and probability density function (PDF) of the spanwise gradient of pressure coefficient, $\Delta C_p/(\Delta z/h)$, on the slant, deck and back for (a) Re1E4, (b) Re5E4, (c) drag coefficient, (d) lift coefficient and (e) drift coefficient for Re1E4 and Re5E4.

These results indicate persistent asymmetry in the flow field, without evidence of mode switching. The absence of bimodality in Re5E4 may be attributed to the timescale ($tU_{\infty}/h \approx 50$) captured in this simulation, as previous studies have reported the emergence of bimodal behavior over much longer timescales (Grandemange et al., 2013b, 2013a; He et al., 2021; Volpe et al., 2015). Furthermore, bimodality has been observed to occur in a stochastic and intermittent manner, which further complicates its detection in computationally intensive simulations.

The instantaneous force coefficients exhibit larger fluctuations and broader PDFs for Re1E4 compared to Re5E4. The PDFs of C_D are centered at 0.468 for Re1E4 and 0.370 for Re5E4, while the

PDFs of C_L are centered at 0.198 and 0.155, respectively. The PDF of C_{Df} is centered at approximately zero for Re1E4, indicating symmetry. For Re5E4, however, the drift is predominantly negative with occasional switches to positive values, resulting in a bimodal PDF characterized by a dominant negative peak at -0.007 and a weaker positive peak at 0.004. This observation suggests the presence of a weak, unstable bimodal behavior in the global wake dynamics of Re5E4, which may not be fully captured by the gradients of the pressure coefficients, perhaps due to rapid switching back to the negative drift state.

3.3.4 Pumping motion of reverse flow regions

The influence of Reynolds number-induced asymmetry on the pumping motion of the recirculation bubbles behind the notchback geometry is investigated using the instantaneous reverse flow area, computed from Equation 3.10 without applying time-averaging. Figures 3.17 and 3.18 present characteristic instantaneous flow fields in the streamwise and spanwise planes, where the reverse flow regions (U < 0) are colored in blue. For each test case, the instantaneous reverse flow regions over the slant and deck are generally larger in the symmetry plane than in the offset planes, while the regions behind the back are typically more extended in the offset planes. Moreover, in the left offset plane of Re5E4, the reverse flow region over the slant is frequently smaller than in the right. In the spanwise planes behind the slant, occasional asymmetry is observed at the slant height for Re1E4 but appears more persistent and pronounced for Re5E4. Behind the back, the reverse flow region often clusters near the sides and may appear disconnected at times. Although this disjointed pattern is also evident in the contours of the streamwise mean velocity (figure 3.6), it primarily results from the cutting plane intersecting sections of the reverse flow volume that are reduced near the symmetry plane due to downwash effects (see figure 3.8). Nonetheless, the reverse flow area computed in the spanwise plane was based on a masked region encompassing all reverse flow clusters.

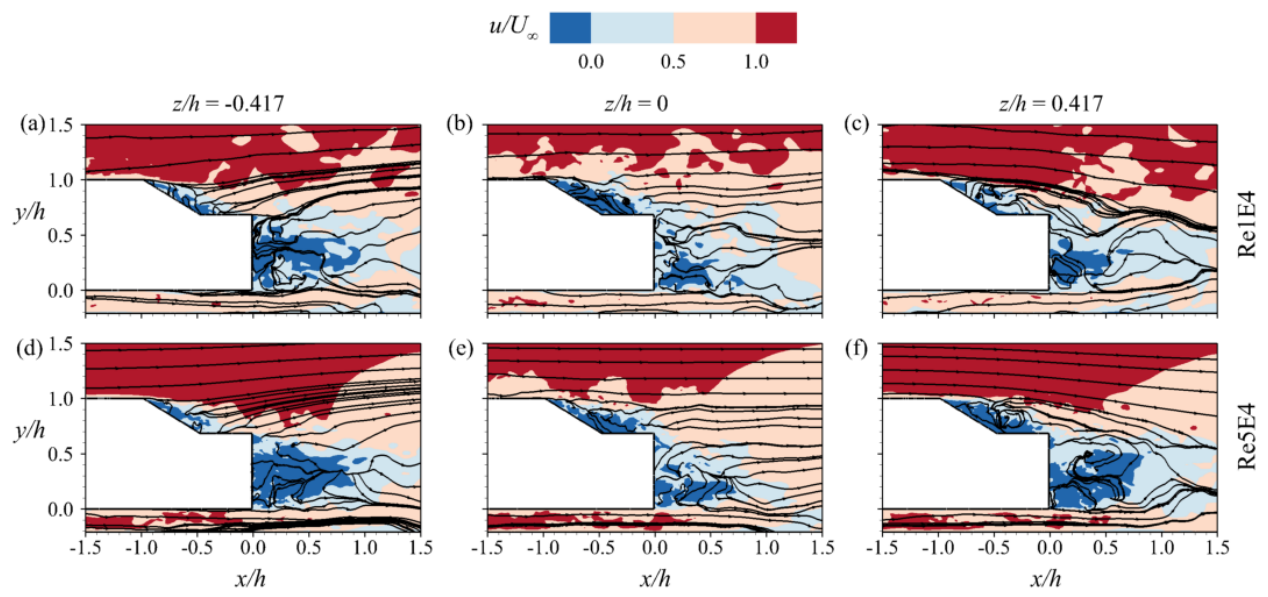


Figure 3.17: Contours of normalized instantaneous streamwise velocity u/U_{∞} in the vertical planes z/h = 0 and $z/h = \pm 0.417$ for Re1E4 and Re5E4, representing a characteristic instantaneous flow field. Blue regions indicate reverse flow areas $(U/U_{\infty} < 0)$ on the slant and at the back of the Ahmed body.

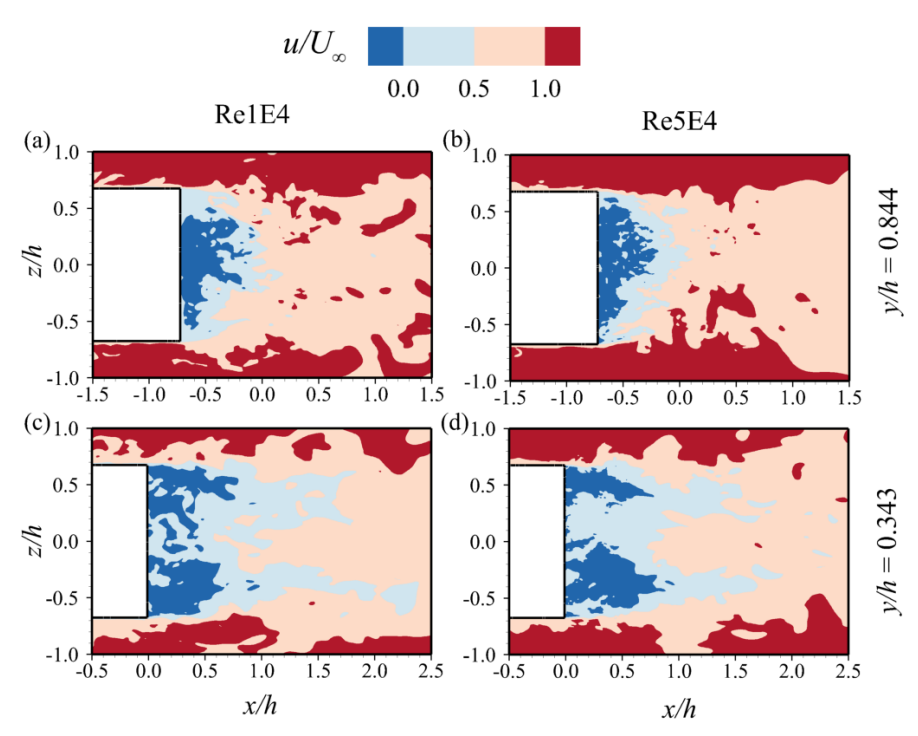


Figure 3.18: Contours of normalized instantaneous streamwise velocity u/U_{∞} in the spanwise planes at (a, b) y/h = 0.844 and (c, b) y/h = 0.343 representing a characteristic instantaneous flow field for Re1E4 and Re5E4. The blue regions indicate reverse flow areas ($U/U_{\infty} < 0$) on the slant and at the back of the Ahmed body.

Figure 3.19 shows the temporal histories and PDFs of the fluctuations of the reverse flow area over the slant and behind the back in the symmetry and offset planes for Re1E4 and Re5E4. Analogous to Reynolds decomposition, the fluctuations of the reverse flow area were determined as $A' = A_t - A$, where A_t is the instantaneous reverse flow area and A is the mean value. Here, A' > 0 demonstrates expansion of the reverse flow region relative to A, while A' < 0 signifies contraction. The skewness (Sk) and kurtosis (K) of A'(t) are shown on the plots to facilitate comparison with a Gaussian distribution, where Sk = 0 and K = 0 indicate perfectly symmetric pumping motion. For Re1E4, the reverse flow region over the slant exhibits more frequent expansion in the symmetry plane, while contractions are more frequent in the offset planes. However, the tails of the PDFs reveal occasionally strong opposite events in each plane. In contrast, the corresponding profiles for Re5E4 indicate symmetric pumping motion in the symmetry plane, but with more frequent contractions on the left plane and expansions on the right plane. This observation is consistent with the presence of a larger mean reverse flow region on the right side of Re5E4, as shown in Figures 3.5 and 3.8. Behind the back, the PDFs in the symmetry plane for both Reynolds numbers are centered near zero. In the offset planes, frequent contractions occur on the left side for both Re1E4 and Re5E4. In contrast, the right side exhibits nearly symmetric pumping for Re1E4, whereas Re5E4 shows frequent expansions. Figure 3.20 shows that the reverse flow regions captured in the spanwise planes exhibit symmetric expansion and contraction behind the slant for both Reynolds numbers. However, behind the back, the PDFs display more frequent contractions and a wider spread of occasional stronger expansions. These expansions may be influenced by spanwise vortex shedding from the sides of the back.

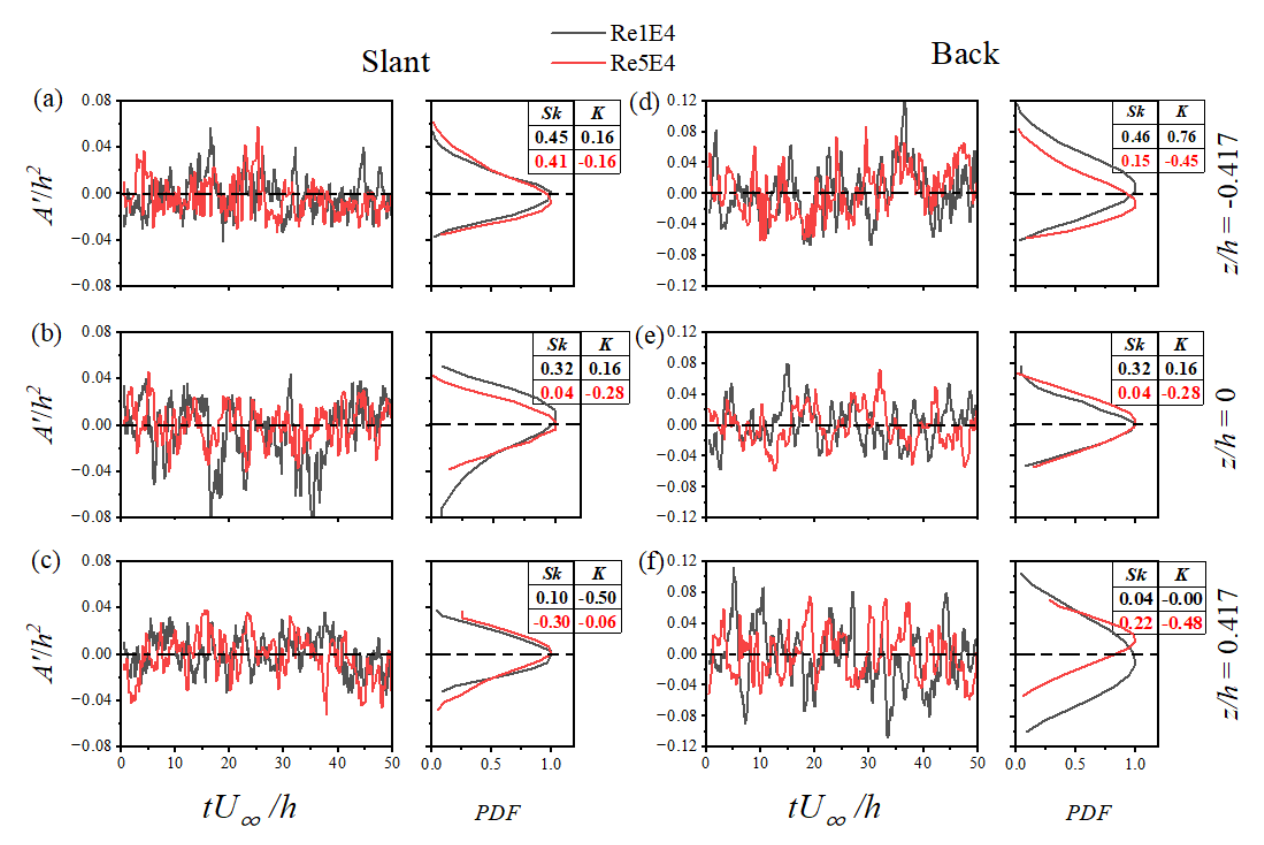


Figure 3.19: Time history and the probability density function (PDF) of the reverse flow area fluctuations (A') on the (a-c) slant and (d-f) back in the vertical planes z=0 and $z/h=\pm 0.417$ for Re1E4 and Re5E4. The parameters Sk and K represent the skewness and kurtosis of A', respectively.

To investigate the interactions between the reverse flow regions over the slant-deck and behind the back, joint probability density functions (JPDFs) of their respective fluctuations are presented in figure 3.21. The JPDF quadrants are labeled Q1 to Q4: Q1 represents synchronized expansion in both regions, while Q3 corresponds to synchronized contraction. Q2 captures events where the reverse flow contracts over the slant but expands behind the back, and Q4 represents the opposite event. For the offset planes of Re1E4, the JPDFs are centered at zero but exhibit a directional preference toward Q1 and Q3, indicating alternating synchronized expansion and contraction between the reverse flow regions over the slant and behind the back. At the symmetry plane, the JPDF is more compact, with a dominant peak in Q1, suggesting more frequent synchronized expansion events between the two regions. In contrast, for Re5E4, the JPDF on the left plane is

skewed toward Q2 and Q4, with a pronounced peak in Q2, implying that frequent contractions of the reverse flow region over the slant are often associated with simultaneous expansion behind the back. On the right side, the JPDF exhibits a vertically aligned structure with dual peaks in Q1 and Q4, suggesting alternating occurrences of synchronized expansion and asynchronous pumping, where frequent expansion over the slant coincides with contraction behind the back. At the symmetry plane, the JPDF for Re5E4 is more evenly distributed across all quadrants, with a marginal peak in Q4. These results indicate that, while the pumping motions over the slant and behind the back are predominantly synchronized in Re1E4, the Reynolds number-induced asymmetry in Re5E4 gives rise to spanwise imbalance and a phase shift in the pumping motion between the reverse flow regions over the slant and behind the back.

To investigate the interactions between the reverse flow regions over the slant-deck and behind the back, joint probability density functions (JPDFs) of their respective fluctuations are presented in figure 3.21. The JPDF quadrants are labeled Q1 to Q4: Q1 represents synchronized expansion in both regions, while Q3 corresponds to synchronized contraction. Q2 captures events where the reverse flow contracts over the slant but expands behind the back, and Q4 represents the opposite event. For the offset planes of Re1E4, the JPDFs are centered at zero but exhibit a directional preference toward Q1 and Q3, indicating alternating synchronized expansion and contraction between the reverse flow regions over the slant and behind the back. At the symmetry plane, the JPDF is more compact, with a dominant peak in Q1, suggesting more frequent synchronized expansion events between the two regions. In contrast, for Re5E4, the JPDF on the left plane is skewed toward Q2 and Q4, with a pronounced peak in Q2, implying that frequent contractions of the reverse flow region over the slant are often associated with simultaneous expansion behind the back. On the right side, the JPDF exhibits a vertically aligned structure with dual peaks in Q1 and

Q4, suggesting alternating occurrences of synchronized expansion and asynchronous pumping, where frequent expansion over the slant coincides with contraction behind the back. At the symmetry plane, the JPDF for Re5E4 is more evenly distributed across all quadrants, with a marginal peak in Q4. These results indicate that, while the pumping motions over the slant and behind the back are predominantly synchronized in Re1E4, the Reynolds number-induced asymmetry in Re5E4 gives rise to spanwise imbalance and a phase shift in the pumping motion between the reverse flow regions over the slant and behind the back.

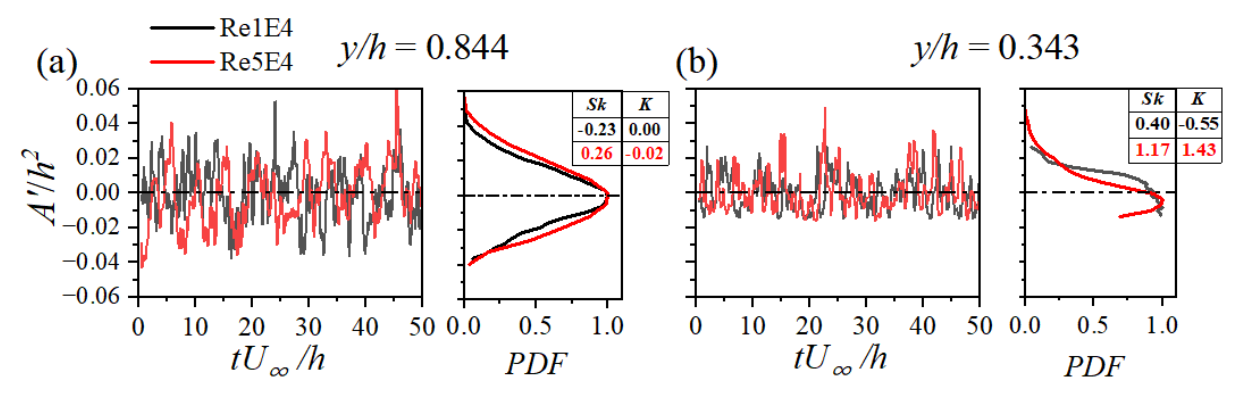


Figure 3.20: Time history and the probability density function (PDF) of the reverse flow area fluctuations on the (a) slant mid-height (y/h = 0.844) and (b) back mid-height (y/h = 0.343) spanwise planes for Re1E4 and Re5E4. The parameters Sk and K represent the skewness and kurtosis of A', respectively.

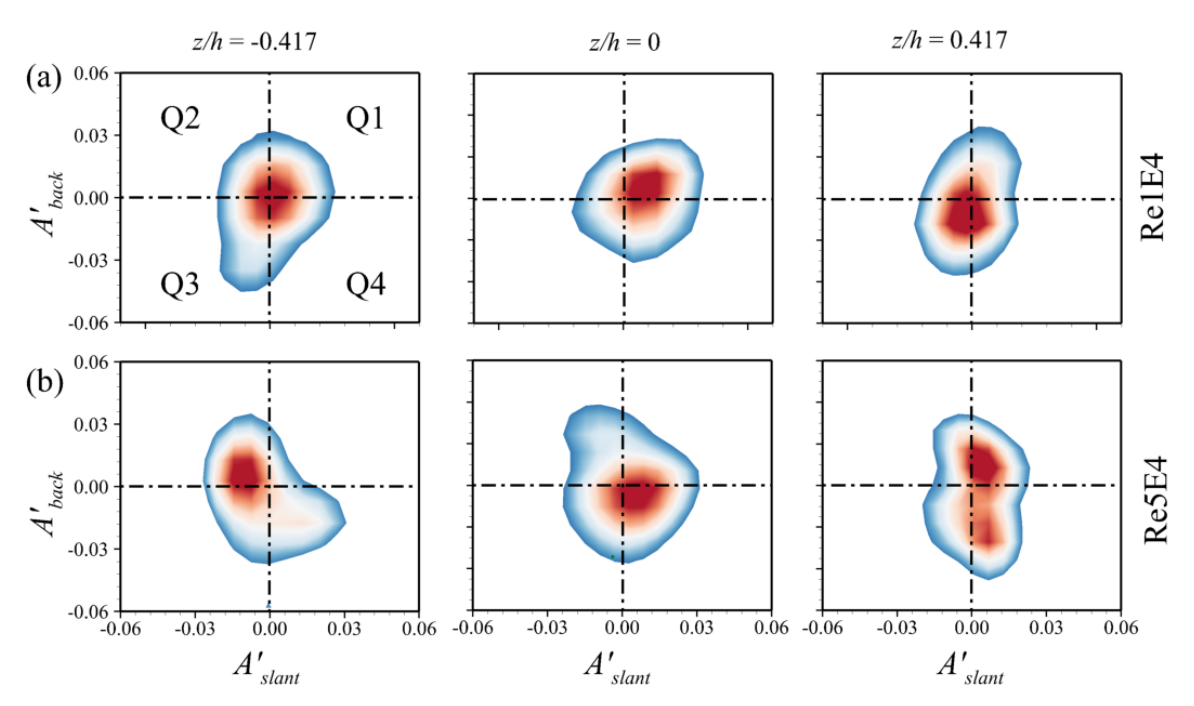


Figure 3.21: Joint probability density function (JPDF) of the fluctuations of reverse flow area on the slant and behind the back in the vertical planes z=0 and $z/h=\pm0.417$ for (a) Re1E4 and (b) Re5E4.

Chapter 4

Conclusion

4.1 Summary

The effect of Reynolds number on the unsteady wake characteristics of a notchback Ahmed body with an effective backlight angle of $\beta_e=17.8^\circ$ was investigated using IDDES. Based on the study by Ouedraogo & Essel (2024), the Reynolds number based on the freestream velocity and body height was set to $Re_h=1\times10^4$ (denoted as Re1E4) and $Re_h=5\times10^4$ (Re5E4) to examine the symmetric and asymmetric wake regimes of the notchback, respectively. The ground clearance ratio was fixed at G/h=0.21.

For both cases, the separated flow from the roof reattached on the deck before subsequently separating at the trailing edge of the deck. However, unlike Re1E4, which demonstrated symmetric reattachment and reverse flow region over the slant, Re5E4 exhibited an asymmetric behavior due to earlier reattachment on the left side compared to the right. The side of earlier reattachment was associated with more pronounced C-pillar, spanwise, and streamwise vortices, which enhanced spanwise entrainment and downwash on the left side compared to the right. Behind the body, the downwash is more intense near the symmetry plane, resulting in redistribution of the reverse flow toward the sides in both test cases. However, for Re5E4, the redistribution is uneven, with a larger reverse flow on the left side than on the right, indicating an asymmetric toroidal structure behind the body.

The turbulence statistics showed significantly higher Reynolds stresses, turbulence production, and large-scale anisotropy for Re5E4 compared to Re1E4. However, for Re5E4, these statistics were more intense in the shear layers on the right side than on the left. Moreover, the asymmetry

in Re5E4 was most pronounced in $\overline{u'u'}$ compared to $\overline{v'v'}$ and $\overline{w'w'}$, as $\overline{u'u'}$ was the dominant contributor to turbulence production. The results also demonstrated the role of the pressure redistribution term in the Reynolds stress transport equation, which was shown to redistribute energy across the Reynolds stress components, from local dominant sources to energy sinks (i.e., regions of negative production) in the other components.

The instantaneous vortical structures, visualized using the *Q*-criterion, and the temporal histories of the spanwise gradients of the pressure coefficients and the drift force coefficient, revealed a directional bias in vortex motion that resulted in the asymmetric wake structure of Re5E4. This asymmetry was more pronounced over the slant-deck region than behind the back. The pumping motion of the reverse flow regions over the slant and behind the back was found to be synchronized for Re1E4, but predominantly out of phase for Re5E4, due to the effects of asymmetric attachment on the deck.

4.2 Recommended future work

The present study employed IDDES to investigate the unsteady turbulent wake characteristics of the notchback Ahmed body at two Reynolds numbers. The effects of Reynolds number on the mean flow, Reynolds stresses, large-scale anisotropy, global instabilities, and the pumping motion in the wake were analyzed. Future work should focus on further exploring more unsteady features such as the frequency spectra of turbulent structures using time-resolved experimental data. This would be essential for validating and improving future numerical simulation models. Additionally, investigations of the effects of flow control strategies, such as the use of synthetic jet actuators, could offer valuable insights and complement the current and previous findings on the notchback Ahmed body.

References

- Ahmed, S. R., Ramm, G., & Faltin, G. (1984). Some Salient Features of the Time-Averaged Ground Vehicle Wake. *SAE Transactions*, **93**, 473–503. http://www.jstor.org/stable/44434262
- Aleyasin, S. S., Tachie, M. F., & Balachandar, R. (2021). Characteristics of flow past elongated bluff bodies with underbody gaps due to varying inflow turbulence. *Physics of Fluids*, **33**(12), 125106. https://doi.org/10.1063/5.0072390
- Bello-Millán, F. J., Mäkelä, T., Parras, L., Del Pino, C., & Ferrera, C. (2016). Experimental study on Ahmed's body drag coefficient for different yaw angles. *Journal of Wind Engineering and Industrial Aerodynamics*, **157**, 140-144.
- Chen, C. W., Wang, S., & Ghaemi, S. (2024). Spectral proper orthogonal decomposition of time-resolved three-dimensional flow measurements in the turbulent wake of the Ahmed body. *Journal of Fluid Mechanics*, **985**, A19. https://doi.org/10.1017/jfm.2024.288
- Chen, G., Li, X. B., He, K., Cheng, Z., Zhou, D., & Liang, X. F. (2023). Effect of the free-stream turbulence on the bi-modal wake dynamics of square-back bluff body. *Physics of Fluids*, **35**(1). https://doi.org/10.1063/5.0134912
- Choi, H., Lee, J., & Park, H. (2014). Aerodynamics of heavy vehicles. *Annual Review of Fluid Mechanics*, **46**, 441–468. https://doi.org/10.1146/annurev-fluid-011212-140616
- Cherry, N. J., Hillier, R., & Latour, M. (1984). Unsteady measurements in a separated and reattaching flow. *Journal of Fluid Mechanics*, **144**, 13–46. https://doi.org/10.1017/S002211208400149X
- Cogotti, A. (1986). Car-Wake Imaging Using a Seven-Hole Probe. *SAE Transactions*, **95**, 1071–1095. http://www.jstor.org/stable/44721731
- Dalla Longa, L., Evstafyeva, O., & Morgans, A. S. (2019). Simulations of the bi-modal wake past three-dimensional blunt bluff bodies. *Journal of Fluid Mechanics*, **866**, 791–809. https://doi.org/10.1017/jfm.2019.92
- Fan, Y., Xia, C., Chu, S., Yang, Z., & Cadot, O. (2020). Experimental and numerical analysis of the bi-stable turbulent wake of a rectangular flat-backed bluff body. *Physics of Fluids*, **32**(10), 105111. https://doi.org/10.1063/5.0019794
- Germano, M., Piomelli, U., Moin, P., & Cabot, W. H. (1991). A dynamic subgrid-scale eddy viscosity model. *Physics of Fluids A: Fluid Dynamics*, **3**(7), 1760–1765. https://doi.org/10.1063/1.857955
- Grandemange, M., Cadot, O., & Gohlke, M. (2012). Reflectional symmetry breaking of the separated flow over three-dimensional bluff bodies. *Physical Review E Statistical, Nonlinear, and Soft Matter Physics*, **86**(3), 1–4. https://doi.org/10.1103/PhysRevE.86.035302

- Grandemange, M., Gohlke, M., & Cadot, O. (2013a). Bi-stability in the turbulent wake past parallelepiped bodies with various aspect ratios and wall effects. *Physics of Fluids*, **25**(9), 095103. https://doi.org/10.1063/1.4820372
- Grandemange, M., Gohlke, M., & Cadot, O. (2013b). Turbulent wake past a three-dimensional blunt body. Part 1. Global modes and bi-stability. *Journal of Fluid Mechanics*, **722**, 51–84. https://doi.org/10.1017/jfm.2013.83
- Gritskevich, M. S., Garbaruk, A. V, Schütze, J., & Menter, F. R. (2012). Development of DDES and IDDES formulations for the k-ω shear stress transport model. *Flow, Turbulence and Combustion*, **88**, 431–449. https://doi.org/10.1007/s10494-011-9378-4
- Guilmineau, E., Deng, G. B., Leroyer, A., Queutey, P., Visonneau, M., & Wackers, J. (2018). Assessment of hybrid RANS-LES formulations for flow simulation around the Ahmed body. *Computers and Fluids*, **176**, 302–319. https://doi.org/10.1016/j.compfluid.2017.01.005
- He, K., Minelli, G., Wang, J., Dong, T., Gao, G., & Krajnović, S. (2021a). Numerical investigation of the wake bi-stability behind a notchback Ahmed body. *Journal of Fluid Mechanics*, **926**, A36. https://doi.org/10.1017/jfm.2021.748
- He, K., Minelli, G., Su, X., Gao, G., & Krajnović, S. (2021b). Influence of the rounded rear edge on wake bi-stability of a notchback bluff body. *Physics of Fluids*, **33**(11), 115107. https://doi.org/10.1063/5.0071925
- He, K., Minelli, G., Su, X., Gao, G., & Krajnović, S. (2021c). Blockage influence on bi-stable flows of a notchback bluff body. *Physics of Fluids*, **33**(12), 125113. https://doi.org/10.1063/5.0077251
- He, K., Minelli, G., Wang, J., Gao, G., & Krajnović, S. (2021d). Assessment of LES, IDDES and RANS approaches for prediction of wakes behind notchback road vehicles. *Journal of Wind Engineering and Industrial Aerodynamics*, **217**, 104737. https://doi.org/10.1016/j.jweia.2021.104737
- He, K., Minelli, G., Su, X., Wang, J., Gao, G., & Krajnović, S. (2022). Floor motion's influence on wake asymmetry of a notchback bluff body. *Physics of Fluids*, **34**(3), 035103. https://doi.org/10.1063/5.0084435
- Hunt, J. C. R., Wray, A. A., & Moin, P. (1988). Eddies, streams, and convergence zones in turbulent flows. *Center for Turbulence Research, Proceedings of the Summer Program*, 193-208.
- Kang, N., Essel, E. E., Roussinova, V., & Balachandar, R. (2021). Effects of approach flow conditions on the unsteady three-dimensional wake structure of a square-back Ahmed body. *Physical Review Fluids*, **6**(3), 034613. https://doi.org/10.1103/PhysRevFluids.6.034613
- Kodie-Ampaw, J. K., Bonsi, A. K., Ouedraogo N.F & Essel, E. E. (2025). The influence of Reynolds number on the turbulent wake regimes of a notchback Ahmed body. *International Journal of Heat and Fluid Flow*. (Under review)

- Kohri, I., Yamanashi, T., Nasu, T., Hashizume, Y., & Katoh, D. (2014). Study on the transient behaviour of the vortex structure behind Ahmed body. SAE International Journal of Passenger Cars-Mechanical Systems, 7(0597), 586-602.
- Krajnović, S., & Davidson, L. (2004). Exploring the flow around a simplified bus with large eddy simulation and topological tools. In R. McCallen, F. Browand, & J. Ross (Eds.), *The Aerodynamics of Heavy Vehicles: Trucks, Buses, and Trains* (pp. 49–64). Springer Berlin Heidelberg.
- Krajnović, S., & Davidson, L. (2005). Flow around a simplified car, part 1: Large eddy simulation. *Journal of Fluids Engineering, Transactions of the ASME*, **127**(5), 907–918. https://doi.org/10.1115/1.1989371
- Ladwig, M., Gericke, T., Huettig, S., & Lindken, R. (2023). Reconstruction of time-averaged 3d pressure fields of an ahmed body with pressure from piv. part i: Scanning stereo-piv. *Symposium on Particle Image Velocimetry. San Diego State University*.
- Launder BE, Reece GJ, & Rodi W. (1975) Progress in the development of a Reynolds-stress turbulence closure. *Journal of Fluid Mechanics*, **68**(3), 537-566. https://doi:10.1017/S0022112075001814
- Leonard, A. (1975). Energy cascade in large-eddy simulations of turbulent fluid flows. In *Advances in geophysics*, **18**, 237–248. https://doi.org/10.1016/S0065-2687(08)60464-1
- Lucas, J. M., Cadot, O., Herbert, V., Parpais, S., & Délery, J. (2017). A numerical investigation of the asymmetric wake mode of a squareback Ahmed body Effect of a base cavity. *Journal of Fluid Mechanics*, **831**, 675–697. https://doi.org/10.1017/jfm.2017.654
- Menter, F. R. (1994). Two-equation eddy-viscosity turbulence models for engineering applications. *AIAA Journal*, **32**(8), 1598–1605. https://doi.org/10.2514/3.12149
- Menter, F. R., & Kuntz, M. (2002). Adaptation of eddy-viscosity turbulence models to unsteady separated flow behind vehicles. In *The aerodynamics of heavy vehicles: trucks, buses, and trains* (pp. 339-352).
- Ouedraogo, N. F., & Essel, E. E. (2024). Effects of Reynolds Number On the Wake Characteristics of a Notchback Ahmed Body. *Journal of Fluids Engineering*, **146**(11), 111302. https://doi.org/10.1115/1.4065225
- Passaggia, P. Y., Mazellier, N., & Kourta, A. (2021). Aerodynamic drag modification induced by free-stream turbulence effects on a simplified road vehicle. *Physics of Fluids*, **33**(10). https://doi.org/10.1063/5.0062232
- Pavia, G., Passmore, M., & Sardu, C. (2018). Evolution of the bi-stable wake of a square-back automotive shape. *Experiments in Fluids*, **59**(1), 20.
- Pearson, D. S., Goulart, P. J., & Ganapathisubramani, B. (2013). Turbulent separation upstream of a forward-facing step. *Journal of Fluid Mechanics*, **724**, 284–304. https://doi.org/10.1017/jfm.2013.113

- Piomelli, U. (1999). Large-eddy simulation: achievements and challenges. *Progress in aerospace sciences*, **35**(4), 335-362. https://doi.org/10.1016/S0376-0421(98)00014-1
- Pope, S. B. (2000). Turbulent flows. Cambridge University Press.
- Prakash, B., Bergada, J. M., & Mellibovsky, F. (2018). Three dimensional analysis of ahmed body aerodynamic performance enhancement using steady suction and blowing flow control techniques. *Tenth International Conference on Computational Fluid Dynamics (ICCFD10)*.
- Ritchie, H., & Roser, M. (2024). Cars, planes, trains: where do CO₂ emissions from transport come from? *Our World in Data*.
- Sarkar, S., & Sarkar, S. (2009). Large-eddy simulation of wake and boundary layer interactions behind a circular cylinder. *Journal of Fluids Engineering*, **131**(9), 091201 https://doi.org/10.1115/1.3176982
- Shur, M. L., Spalart, P. R., Strelets, M. K., & Travin, A. K. (2008). A hybrid RANS-LES approach with delayed-DES and wall-modelled LES capabilities. *International Journal of Heat and Fluid Flow*, **29**(6), 1638–1649. https://doi.org/10.1016/j.ijheatfluidflow.2008.07.001
- Siddiqui, N. A., & Agelin-Chaab, M. (2022). Flow features of the Ahmed body at a low Reynolds number. *International Journal of Heat and Fluid Flow*, **98**, 109052. https://doi.org/10.1016/j.ijheatfluidflow.2022.109052
- Siemens Digital Industries Software. (2020). Simcenter STAR-CCM+ (Version 2020.2) [Computer software]. Siemens
- Sims-Williams, D., Marwood, D., & Sprot, A. (2011). Links between Notchback Geometry, Aerodynamic Drag, Flow Asymmetry and Unsteady Wake Structure. *SAE International Journal of Passenger Cars Mechanical Systems*, **4**(1), 156–165. https://doi.org/10.4271/2011-01-0166
- Smagorinsky, J. 1963. General Circulation Experiments with the Primitive Equations: Part I, The Basic Experiment. *Monthly Weather Review*, **91**, pp. 99-164
- Spalart, P., & Allmaras, S. (1992). A one-equation turbulence model for aerodynamic flows. *30th Aerospace Sciences Meeting and Exhibit*, 439. https://doi.org/doi:10.2514/6.1992-439
- Spalart, P. R. (1997). Comments on the Feasibility of LES for Wings and on the Hybrid RANS/LES Approach. *Proceedings of the First AFOSR International Conference on DNS/LES*, 1997, 137–147.
- Spalart, P. R., Deck, S., Shur, M. L., Squires, K. D., Strelets, M. K., & Travin, A. (2006). A new version of detached-eddy simulation, resistant to ambiguous grid densities. *Theoretical and Computational Fluid Dynamics*, **20**, 181–195. https://doi.org/10.1007/s00162-006-0015-0
- Strachan, R. K., Knowles, K., & Lawson, N. J. (2007). The vortex structure behind an Ahmed reference model in the presence of a moving ground plane. *Experiments in Fluids*, **42**(5), 659–669. https://doi.org/10.1007/s00348-007-0270-x

- Tombazis, N., & Bearman, P. W. (1997). A study of three-dimensional aspects of vortex shedding from a bluff body with a mild geometric disturbance. *Journal of Fluid Mechanics*, **330**, 85–112. https://doi.org/10.1017/S0022112096003631
- Tunay, T., Sahin, B., & Akilli, H. (2013). Experimental and numerical studies of the flow around the Ahmed body. *Wind and Structures*, **17**(5), 515–535.
- Vino, G., Watkins, S., Mousley, P., Watmuff, J., & Prasad, S. (2005). Flow structures in the nearwake of the Ahmed model. *Journal of Fluids and Structures*, **20**(5), 673–695. https://doi.org/10.1016/j.jfluidstructs.2005.03.006
- Volpe, R., Devinant, P., & Kourta, A. (2015). Experimental characterization of the unsteady natural wake of the full-scale square back Ahmed body: flow bi-stability and spectral analysis. *Experiments in Fluids*, **56**(5), 99. https://doi.org/10.1007/s00348-015-1972-0
- Wieser, D., Nayeri, C. N., & Paschereit, C. O. (2020). Wake structures and surface patterns of the drivaer notchback car model under side wind conditions. *Energies*, **13**(2). https://doi.org/10.3390/en13020320